Supporting Information

Heterostructure from heteromixture: Unusual OER activity of FeP and CoP nanostructures on physical mixing

Divya Bhutani,[a] Sisir Maity,[a] Shashank Chaturvedi,[b,c] Divya Chalapathi,[c] Umesh V. Waghmare,[b] Chandrabhas Narayana,[c] Vinod C. Prabhakaran,[d] and Eswaramoorthy Muthusamy,[a]

[a]Chemistry and Physics of Materials Unit, School of Advanced Materials (SAMat), Jawaharlal Nehru Centre for Advanced Scientific Research (JNCASR), Jakkur P.O., Bengaluru 560064, India. E-mail: eswar@jncasr.ac.in; Fax: +91-80-2208-2766.

[b]Theoretical Science Unit, School of Advanced Materials (SAMat), Jawaharlal Nehru Centre for Advanced Scientific Research (JNCASR), Jakkur P.O., Bengaluru 560064, India.

[c]Chemistry and Physics of Materials Unit, School of Advanced Materials (SAMat), Jawaharlal Nehru Centre for Advanced Scientific Research (JNCASR), Jakkur P.O., Bengaluru 560064, India.

[d]Catalysis Division and Center of Excellence on Surface Science, CSIR-National Chemical Laboratory, Pune 411008, India.

Table of contents

1. Experimental section:

1.1 Materials

Cobalt chloride hexahydrate ($CoCl_2.6H_2O$) and anhydrous ferric chloride ($FeCl_3$) were purchased from S D Fine Chemicals, $NaBH_4$, NaH_2PO_2 and 5 wt % Nafion® perflourinated resin solution purchased from Sigma-Aldrich, HCl (37%, AR grade) and KOH from Merck Chemicals. All chemicals were used as received without any further purification. Milli Q water (18.2 S cm) is used for all the synthesis and electrochemical analyses. Toray carbon paper (TGP-H-60) used for electrochemical studies was purchased from Alfa Aesar.

1.2 Catalyst Synthesis

FeP and CoP were individually synthesized by a two-step procedure. Firstly, 30 mL of 0.1 M metal chloride solution was rapidly added to freshly prepared 150 mL of 1.0 M aqueous $NaBH_4$ solution under vigorous stirring. The solution was stirred for another 30 minutes. The product obtained was washed three times with water and ethanol and then dried at 60 ^oC in oven overnight.[1, 2] In the second step, nanostructured metal phosphides were synthesized according to previously reported procedure.[3] In a typical synthesis, 200 mg of as-synthesized metal hydroxide was ground with 1 g of NaH_2PO_2 in a mortar-pestle and heated at 300 ^oC for 1 h in Ar atmosphere (heating and cooling rates were 3 ^oC per minute). Then, the solid product obtained was dispersed in 120 ml 0.1 M HCl solution and stirred for 3 h to remove unreacted metal particles formed during the synthesis of metal hydroxide. The remaining solid product was washed several times with water and ethanol and dried overnight at 60 ^oC in oven. For the synthesis of bimetallic cobalt-iron hydroxides, CoFeP, individual solutions of cobalt and iron chloride were mixed according to their desired compositions (20: 80 wt. % of Co: Fe) and same procedure was followed. Also, the physically ground mixtures [FeP-CoP-(x:y), x and y being the percentage weight ratios of amount of FeP and CoP] were prepared by mixing and grinding required weight ratios of individually synthesized metal phosphides.

1.3 Characterization Techniques and Instrumentation

Powder X-ray diffraction (PXRD) were recorded using Rigaku diffractometer using Cu Kα radiation, (λ=1.54 Å, step size: 0.02, current: 30 mA and voltage: 40 kV). The crystallite size observed from PXRD is determined using Scherrer equation given as:

$\tau=(k\lambda)/(\beta\cos\theta)$,

where τ, k, λ, β, and θ are crystallite size, shape factor (=1), wavelength of source (0.154 nm), full width half maxima (FWHM), and Bragg's angle respectively.

Field-emission scanning electron microscopy (FESEM) images and energy-dispersive X-ray spectroscopy (EDS) were obtained by using FEI (Nova-Nano SEM-600 Netherlands) equipment. Transmission electron microscope (TEM) imaging was done using TALOS F200 S G2 electron microscope operating at an accelerating voltage of 200 kV. Samples were prepared by drop casting a very dilute dispersion of the powdered sample (in absolute ethanol) on a TEM grid (carbon polymer, 300 mesh). Further, to ascertain the composition of Fe and Co in the samples, inductive coupled plasma optical emission spectroscopy (ICP-OES) was carried out using a Perkin−Elmer Optima 7000 DV instrument. X-ray photoelectron spectroscopy (XPS) has been performed using Omicron EA 125 spectrometer with Al K_α (1486.6 eV) source. A Raman micro-spectroscopy system (LabRam HR Evolution, Horiba) with an open electrode CCD air-cooled to -60 ^oC was used to obtain the Raman spectra. The Raman spectra were collected by mapping random areas of the powdered sample placed on a glass slide, using a 50x objective to focus the laser beam to an approximate diameter of 1 μm. The Raman scattering generated with about 3mW of 633 nm radiation in the spectral range of 100-700 cm^{-1} was collected for 300 s per window of the spectrum using an 1800 grooves/mm diffraction grating, using the LabSpec software.

Electrochemical measurements were carried out using electrochemical workstation (660C, USA) obtained from CH instruments for evaluating the electrochemical activities of catalysts towards oxygen evolution reaction (OER), hydrogen evolution reaction (HER), overall water splitting and other electrochemical analyses.

1.4 Electrochemical Measurements

1.4.1 Fabrication of electrodes

The electro active material (2 mg) was dispersed in 0.5 mL mili Q water. Also, 5 μL of 5 wt.% nafion solution added to the resultant dispersion was ultrasonicated to obtain a homogeneous catalyst ink. Then, 2 μL of as obtained catalyst ink was drop casted on a clean glassy carbon (GC) electrode having a diameter of 3 mm resulting in a catalyst loading of 0.112 mg cm^{-2}. The coated GC electrode was dried in ambient conditions and used as working electrode in the electrochemical studies. Toray Carbon paper (0.5*0.5 cm) was used for stability studies at high current densities and for full cell studies.

1.4.2 Electrochemical setup

Electrochemical measurements were carried out using a standard three-electrode cell with a high surface area graphite rod as a counter electrode, mercury-mercuric oxide (Hg/HgO) electrode as a reference electrode in alkaline medium (1 M KOH) in an alkaline cell. The polarization curves are reported with 100% iR compensation which arises due to ohmic resistance of the cell. All the measured potentials are reported with respect to reversible hydrogen electrode (RHE). The obtained current densities were normalized to the geometrical surface area of the GC electrode (0.07068 cm^2). The linear sweep voltammograms (LSVs) were recorded in 1 M KOH at 5 mV s^{-1} under Ar saturated aqueous electrolytes. The Tafel plots were obtained from the polarization curves using Tafel relation considering log(*j*) vs. V. For evaluation of electrochemical double layer capacitance (C_{dl}), cyclic voltammograms (CV) were

recorded at different scan rates (20-100 mV s^{-1}) within the potential range from 1.1 to 1.35 V (vs. RHE). The electrochemically active surface area (ECSA) was calculated from C_{dl} value using the relation,

$$ECSA = C_{dl}/C_s,$$

where C_s is specific capacitance of flat electrode surface (40 μF cm^{-2}).[4] Electrochemical impedance spectroscopy (EIS) studies were performed in frequency range of 0.01 Hz to 100 kHz with an amplitude of 5 mV at various fixed potential values. The cyclic voltammetry (CV) before the polarisation scan is recorded in potential range of 1.05 to 1.35 V (vs. RHE) at a scan rate of 100 mV s^{-1}. Mott-Schottky analysis was studied in anodic potential range of 0.3 to 1.7 V (vs. RHE) at 5 mV s^{-1}.

1.4.3 Electrochemical circuit fitting parameters analysis:

There are three circuits considered to fit the EIS data as shown below. The highly probable fitted circuit for the EIS study is represented in circuit-3 wherein three different relaxation processes can be observed viz. RC contribution to compact layer, charge transfer, and adsorption of reaction intermediates at the surface.[5]

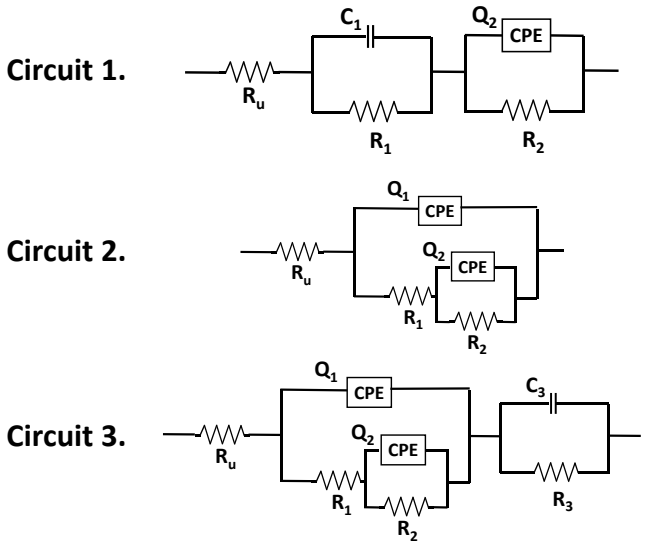

Herein, resistance (R), capacitance (C), and constant phase element (CPE) are considered as active electrical elements. As there is depressed circle observed, the capacitor is replaced by constant phase element (CPE). Ru is the resistance offered by the solution and other components of the cell. RCPE1 corresponds to RC circuit elements linked with compact layer formation as these are not much affected on changing the samples. RCPE2 can be assigned to the RC circuit elements for charge transfer and double layer formation as seen from fitting of circuit-3 for the mixture (Fig S12). Also, as seen from the Tafel behaviour, the Rct values matches well with observed order of FeP-CoP<CoP<FeP. The RC3 can be linked to the adsorption of intermediate species as the C3 values also show the order of FeP-CoP>CoP>FeP.

Various reports suggest circuit-1 for similar sort of EIS data wherein, two RC circuits are connected in series with a solution resistance.[6] While fitting the data in circuit 1, the error with the electrochemical circuit fitting (ECF) is around 3 %. So, shifting to circuit 2 gives very odd fitting with error of 4.5 %. Finally, circuit-3 fits very well with all the samples with error in range of 1 % to 1.7%. All these elements show the effective contribution from the electrochemical structure formed during the reaction.

1.4.4 Calculation of relative charge carrier concentration from Mott-Schottky analysis:

Mott-Schottky analysis deals with interpreting the electrochemical behaviour of the surface of a material immersed in solution.[7] Due to the dangling bonds of the surface-active species, there exist surface states in addition to electron energy bands and impurity levels. To attain the equilibrium between fermi level of surface (containing surface states) and the interior of the material with active interface, there is transfer of charge carriers. If the material is semiconducting, there is generation of an opposite charge but equal in magnitude inside the material, forming near the surface, a space charge layer (SCL). As the two levels equilibrate,

there is bending of bands near the surface in the space charge layer which develops an electrostatic potential which can be explained in terms of double layer model.[7] There are three different layers contributing towards electrochemical activity, viz. space charge layer inside the semiconductor, compact layer (CL) comprising of adsorbed solvent molecules at the surface, and diffusion layer (DL) consisting of solvated ions. The arrangement of the charge carriers leads to existence of parallel plate capacitance in these three regions and the contribution from C_{SC} (capacitance from space charge layer) would be more for the resultant capacitance value in comparison to the other two according to the equation, ($1/C_T = 1/C_{SC} + 1/C_w + 1/C_d$), where C_s, C_w, and C_d are capacitance due to SCL, CL, and DL respectively. This value of C_{SC} can be interpreted with respect to applied potential (V-Vb) by Mott-Schottky equation, ($1/C_s^2 = 2(V-V_b)/N$).

The value of slope will provide the charge carrier concentration (N) and the type of slope (either negative or positive) will deliver the information whether the surface behaves as p-type or n-type. Also, the C vs. V plot tells about the behaviour of the material at the interface in an electrolyte, herein, depicted as a leaky MOS capacitor (Fig S22).

1.4.5 Calibration of Reference Electrode:

The reference electrodes, Hg/HgO used in alkaline electrolyte (KOH solution) was calibrated with respect to reversible hydrogen electrode (RHE) using large area Pt foil as a working electrode and Pt coil as counter electrode. High purity hydrogen gas was purged in the electrolyte for 45 minutes before the experiment to achieve H_2 saturation and a constant purging of H_2 was maintained during the measurement. Cyclic voltammograms were recorded at a scan rate of 1 mV s^{-1}. The average of potential values (at j=0) for the forward and backward scans (HER and HOR respectively) were considered as the standard potential of the reference (vs. RHE).[8] The calibration plots are given in Fig. S9.

For 1 M KOH, $E_{RHE} = E_{Hg/HgO} + 0.930$ V

1.4.6 Calculation of Faradaic Efficiency and turn over frequency (TOF):

Faradaic efficiency (FE) of a reaction determines the selectivity of the reaction towards formation of a particular product. Here, the faradaic efficiency of OER was determined by water-gas displacement method wherein; a burette is inverted in water and the O_2 gas coming out from the anodic chamber of airtight H-type electrochemical cell containing the working electrode (catalyst coated GC) and reference electrode (Hg/HgO) displaces the water in the burette. The amount of water displaced equals to the amount of gas evolved. The experiment was performed under potentiostatic conditions at 1.53 V vs. RHE and the amount of observed charge was compared with that observed from the volume of water replaced by the evolved O_2 by using the following relation:

$FE = (Q_{O_2}/Q_{total})*100$,

where Q_{O_2} and Q_{total} are experimentally observed charge and total theoretical charge associated with O_2 evolution respectively.

$Q_{O_2} = (N_{O_2})/(n*F)$, where N_{O_2} is number of moles of O_2 evolved, n = number of electrons transferred (4 for OER), and F (Faraday's constant) = 96485 C mol^{-1}.

$N_{O_2} = V/V_m$, where V is volume of water displaced, and V_m (molar volume) = 22.4 L.

3.6 mL of O_2 gas was collected in the inverted burette corresponding to $Q_{O_2} = 62.03$ C.

Q_{total} is calculated from the charge observed via potentiostatic measurement for 7200 s at 1.53 V vs. RHE and equals to 63.77 C. Thus, the faradaic efficiency comes out to be 97%.

Further, the TOF values for different catalysts were calculated from the following relation:

$TOF = (j*A)/(n*F*m)$,

where j is current density at a fixed potential, A is geometrical surface area (0.07068 cm^{-2}), n is the number of electrons transferred (n=4, for OER), F is Faraday constant (96485 C), and m is moles of active metal sites. The number of moles of active species is calculated from the amount of metal species coated on the working electrode as:

$m = w/M_W$,

where w is weight of metals taken in the sample and M_W is the molecular weight of metals in the sample.[9]

1.4.7 Purification of KOH solution:

Commercial grade KOH which contains trace amount of Fe (~ 1ppm, analyzed by ICP-OES measurement) was purified by using $Co(OH)_2$ absorption method reported in the literature.[10] In a typical procedure, 2 g of $Co(NO_3)_2$ was dissolved in 4 mL mili Q water followed by the addition of 20 mL of 0.1 M KOH solution (with stirring for 5 minutes) to synthesize $Co(OH)_2$. The separation of $Co(OH)_2$ precipitates was carried out by centrifugation and washing with mili Q water (5 times). The obtained $Co(OH)_2$ was used for purification of KOH. Mechanical agitation (10 minutes) was carried out for a mixture of as-prepared $Co(OH)_2$ and 50 mL 1 M KOH solution to absorb Fe impurities. Then the brown colored suspension was removed by centrifugation for 1 h and the purified KOH was separated out. The process was repeated for another three times with the same purified KOH solution and finally used as Fe-free KOH electrolyte for electrochemical measurements. Also, the absence of Fe in 1 M KOH solution was confirmed by ICP-AES analysis.

1.4.8 DFT calculations: Computational details

We used Quantum ESPRESSO software package[11] to perform density functional theoretical calculations. We also performed NEB calculations to understand the potential determining step. To model ion-electron interaction we used projector-augmented wave (PAW) potentials. We used generalized gradient approximation as given by Perdew-Burke-Ernzerhof (PBE).[12, 13] We also included Grimme-D2 corrections to account for van der Waals interactions[14]. A uniform mesh of 6×6×1 k-points[15] was used in sampling of Brillouin-zone (BZ) integrations. To model slab, we used a vacuum of 15 Å to prevent the interaction between periodic images.

1.5 Figures

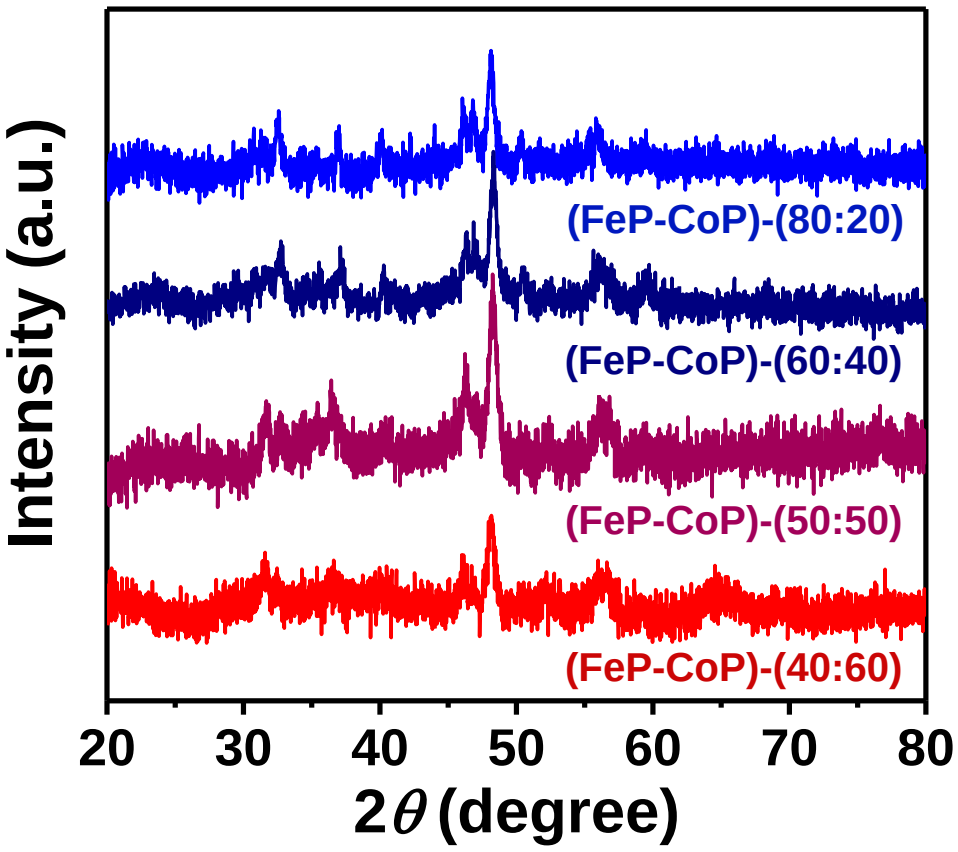

Fig. S1 PXRD pattern of mixtures of FeP and CoP in different compositions.

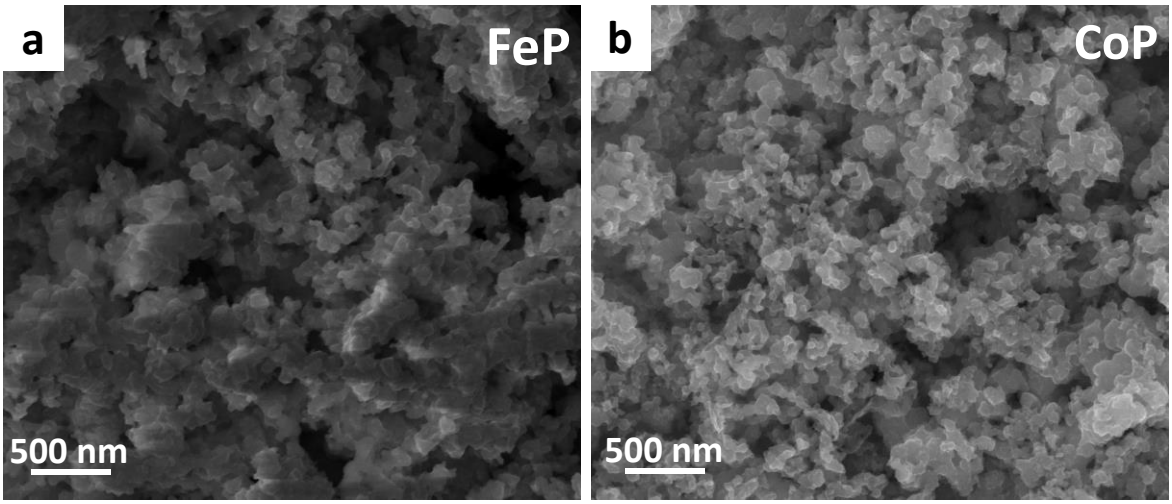

Fig. S2 FESEM of FeP, and CoP.

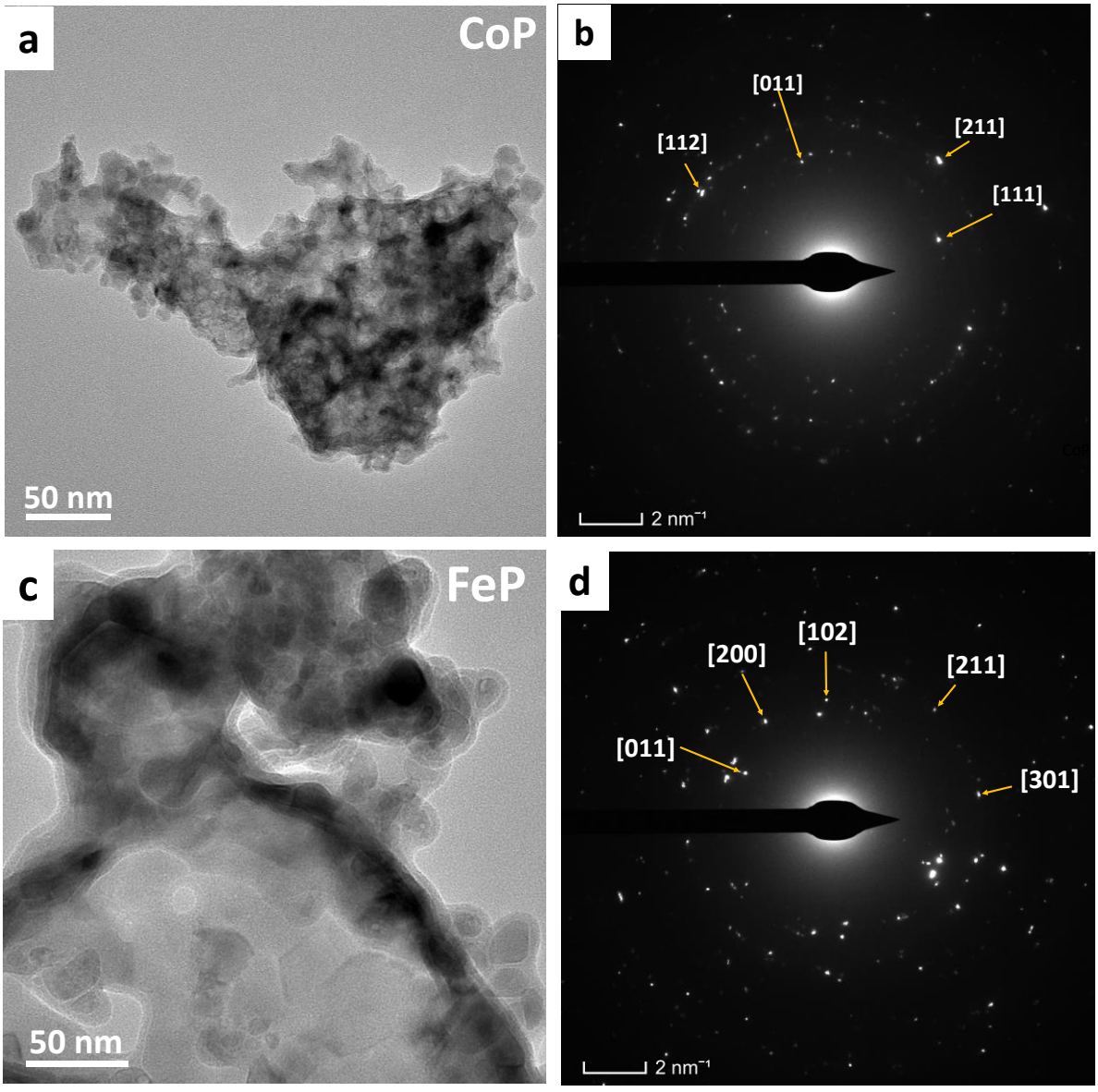

Fig. S3 (a, c) TEM image, and (b,d) SAED pattern of CoP and FeP, respectively.

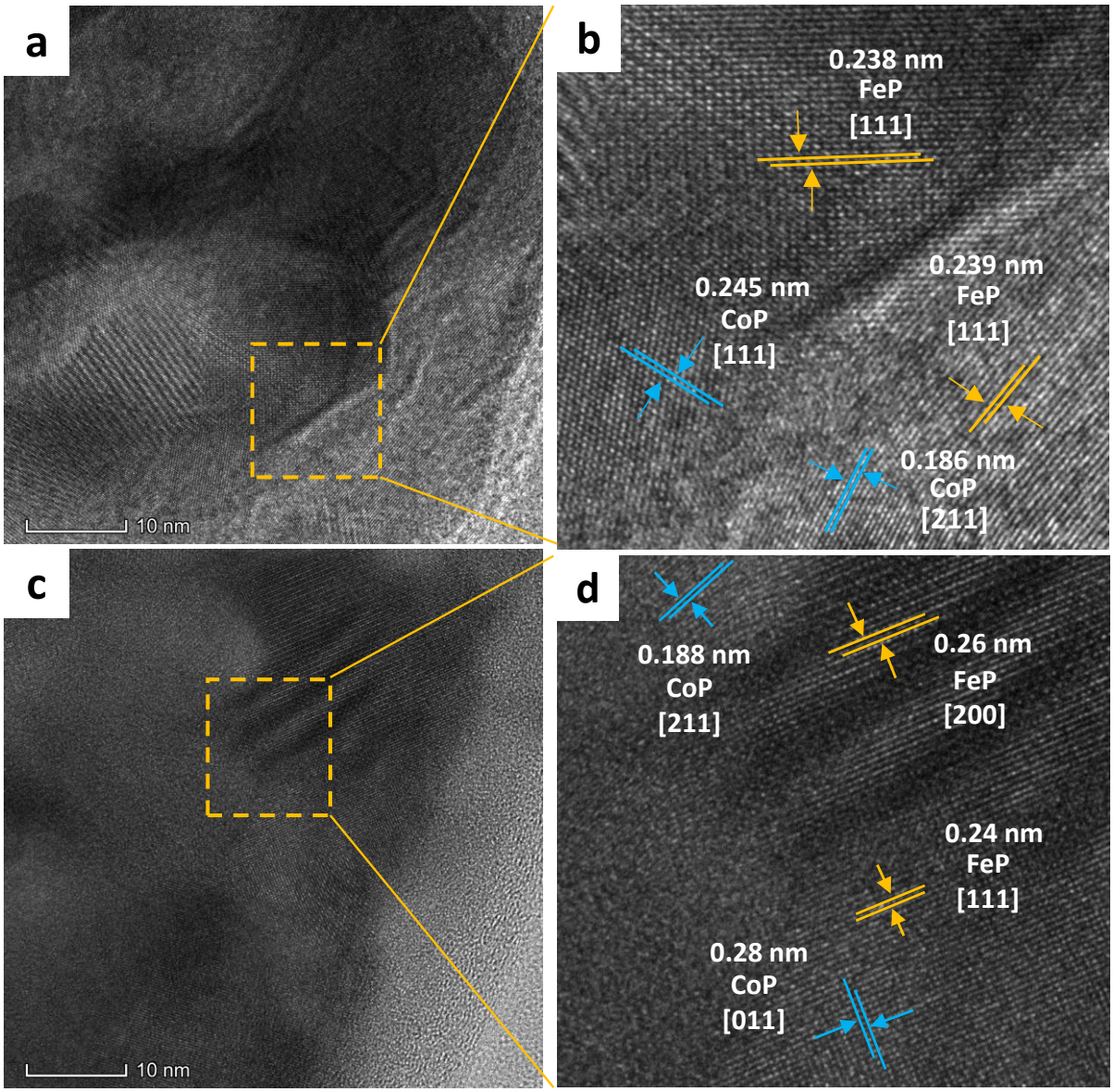

Fig. S4 (a-d) HRTEM of (FeP-CoP) catalyst.

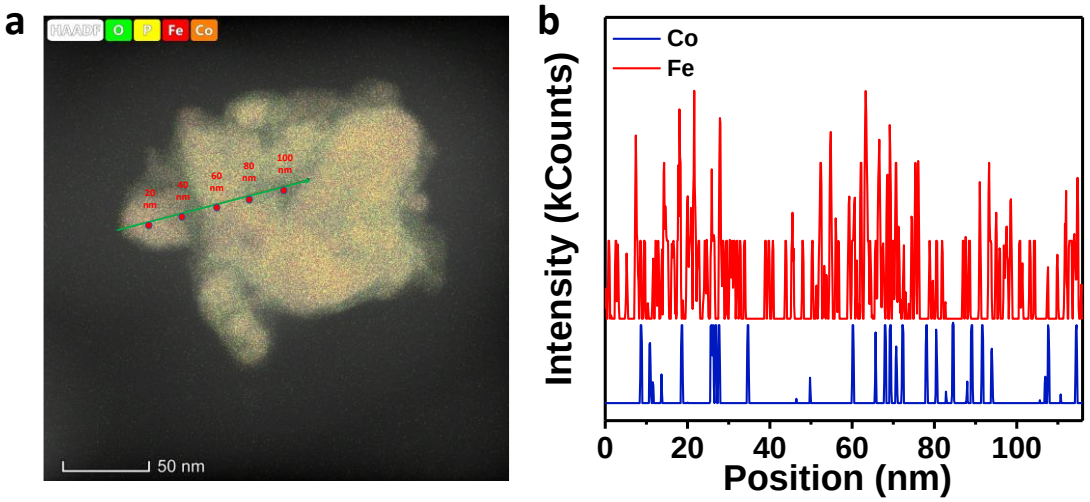

Fig. S5 (a) HAADF-STEM, and (b) line mapping profile of Co, and Fe in (FeP-CoP) catalyst.

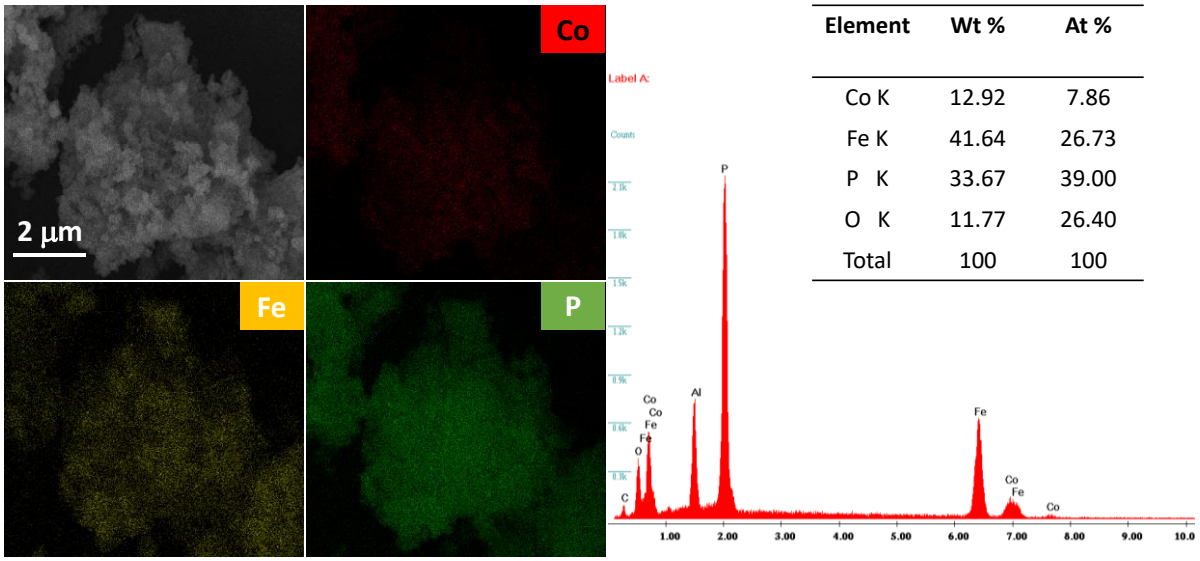

Element	Wt %	At %
Co K	12.92	7.86
Fe K	41.64	26.73
P K	33.67	39.00
O K	11.77	26.40
Total	100	100

Fig. S6 EDS elemental mapping of (FeP-CoP) catalyst.

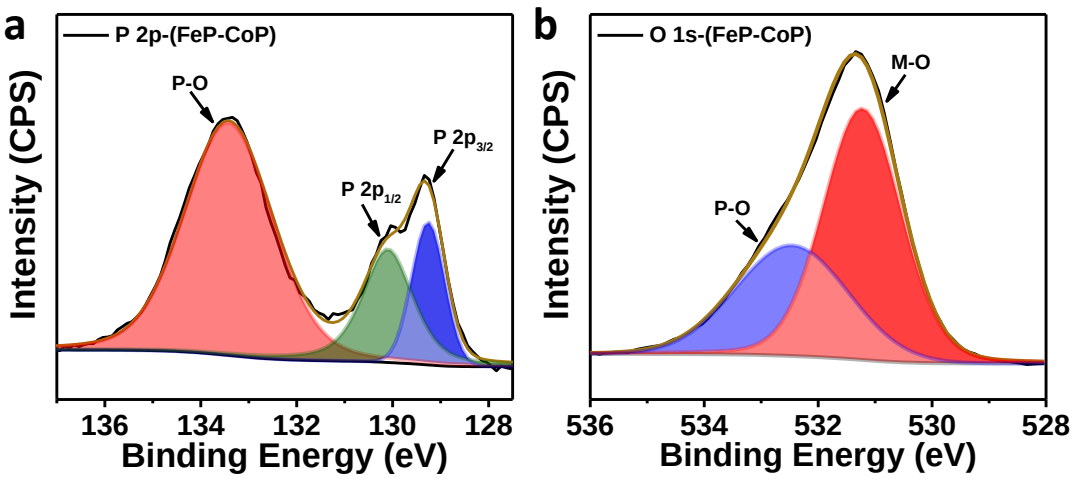

Fig. S7 High resolution XPS spectra of (a) P 2p and (b) O 1s of (FeP-CoP) catalyst.

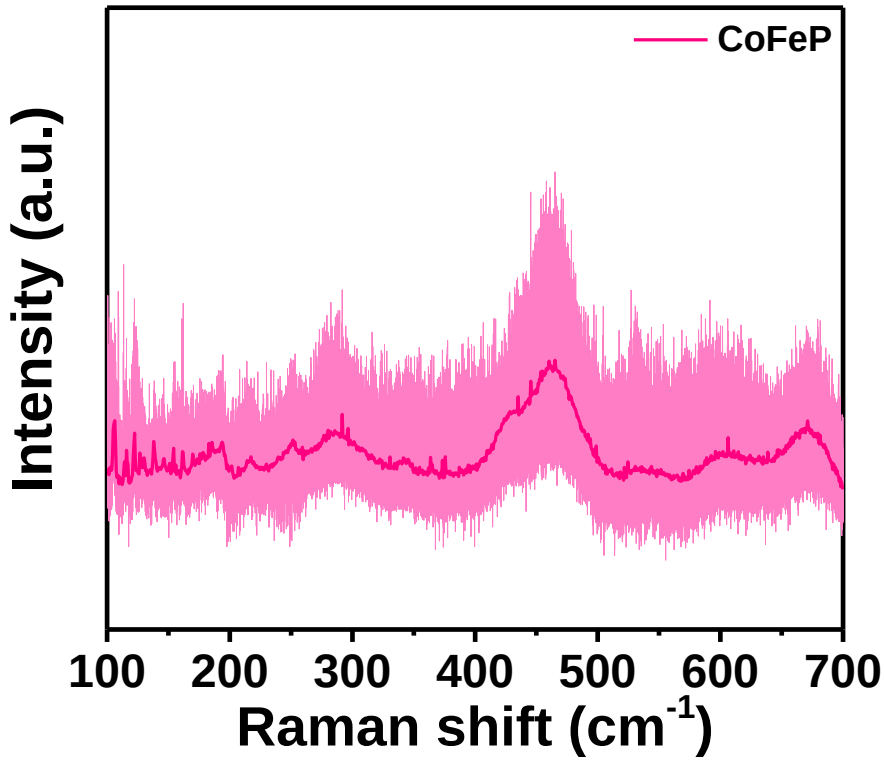

Fig. S8 Raman spectra of in-situ synthesized CoFeP catalyst.

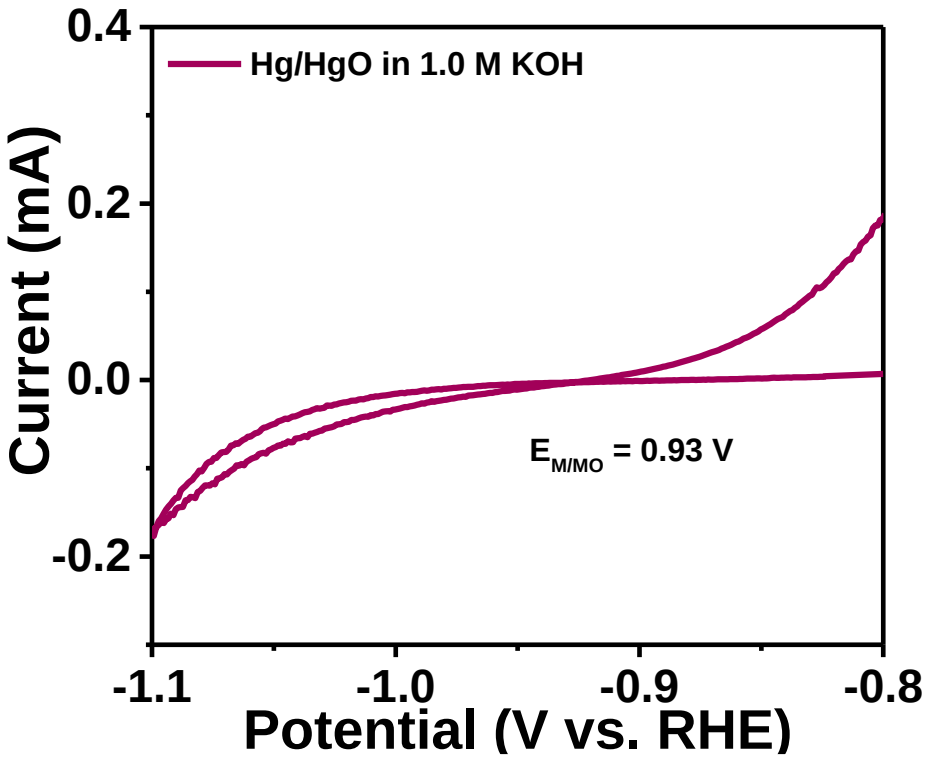

Fig. S9 Calibration plot of Hg/HgO reference electrode in 1.0 M KOH electrolyte.

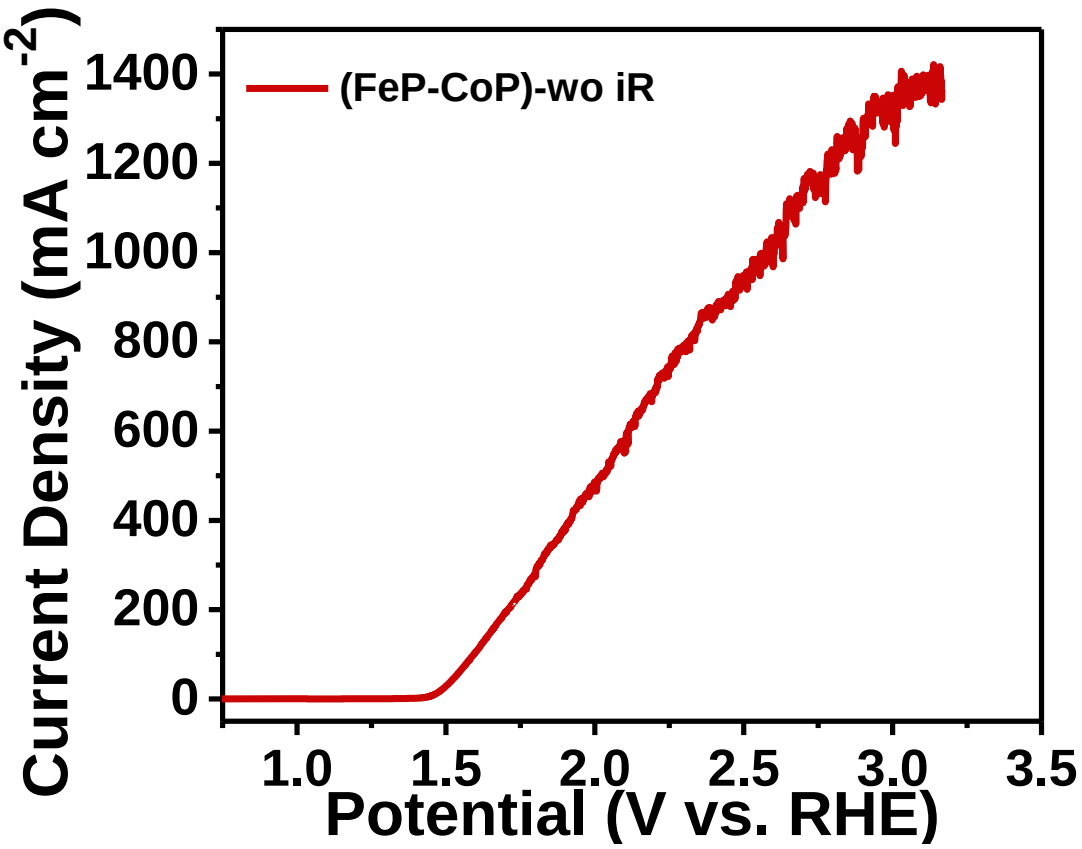

Fig. S10 LSV of FeP-CoP catalyst without iR compensation.

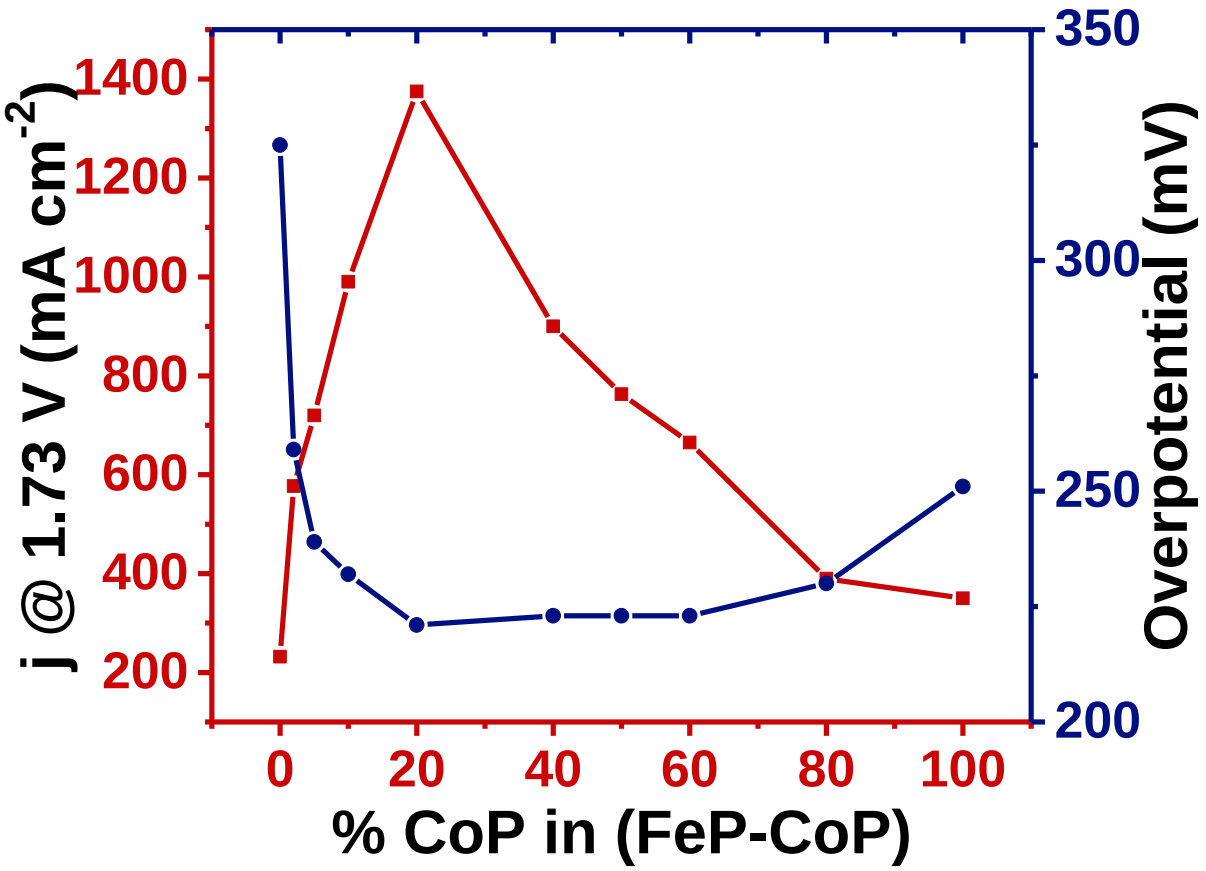

Fig. S11 Electrochemical activity of different compositions of mixtures of CoP in FeP. (*j* is current density)

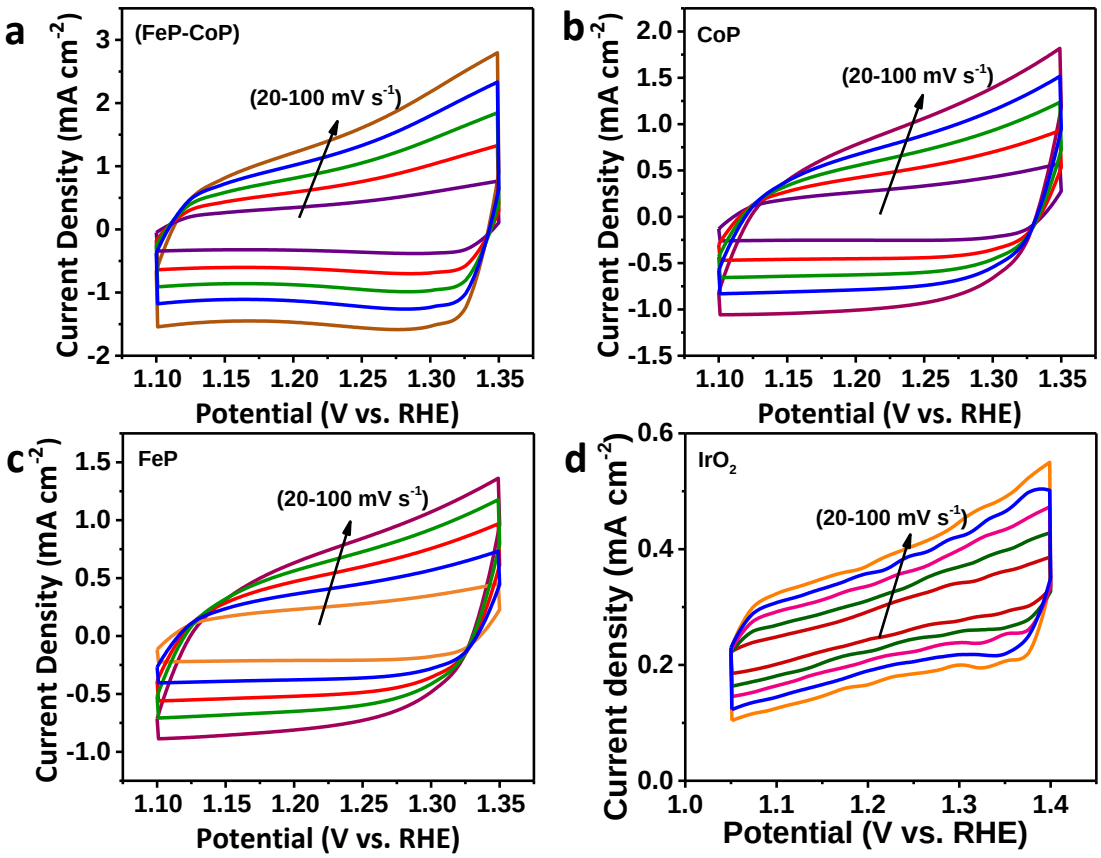

Fig. S12 Cyclic voltammograms (CV) of different catalysts in non-faradaic region.

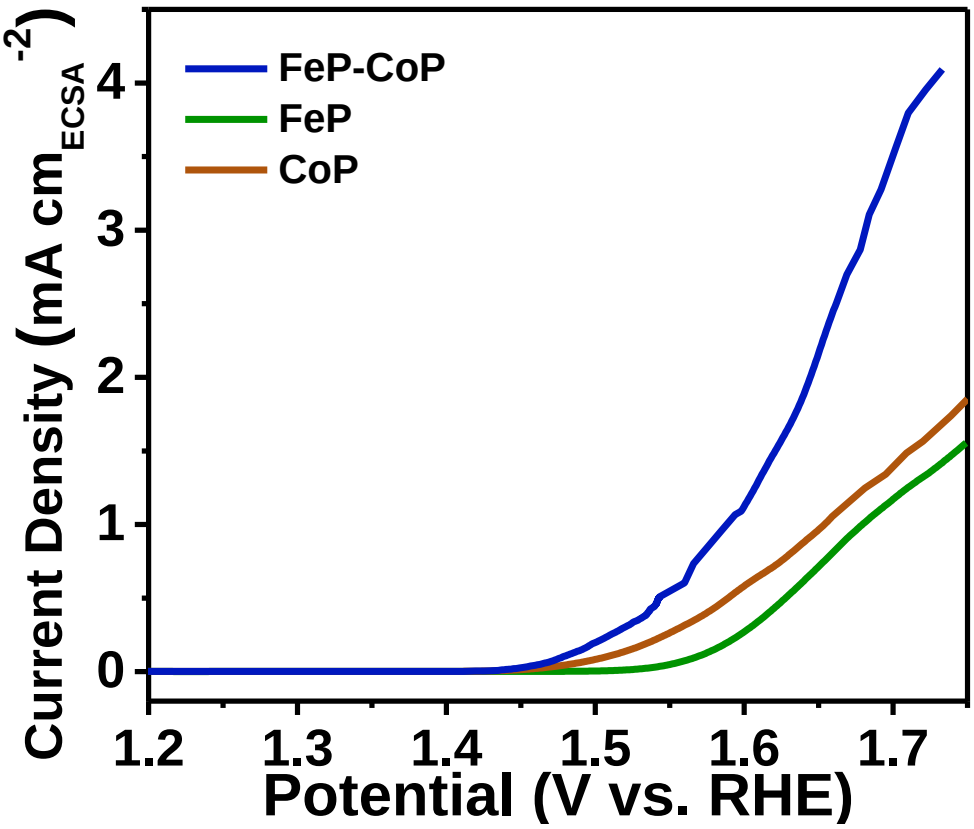

Fig. S13 LSV of FeP, CoP and FeP-CoP catalysts with current normalized to corresponding ECSA values.

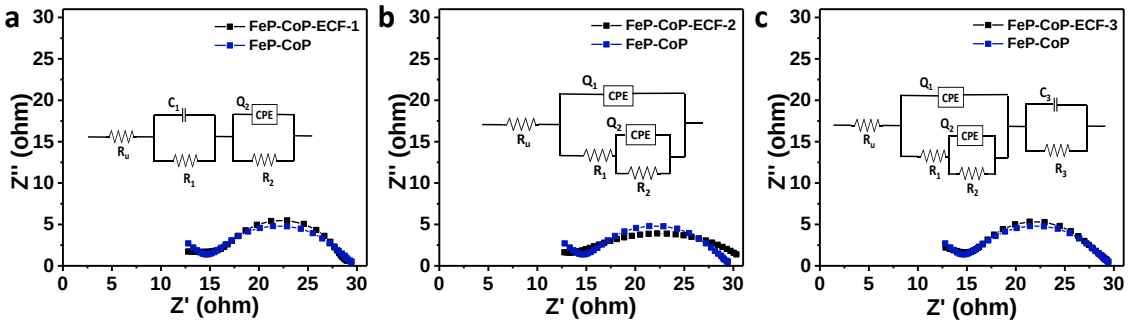

Fig. S14 (a-c) Electrochemical impedance Circuit fitting (ECF) of FeP-CoP catalyst.

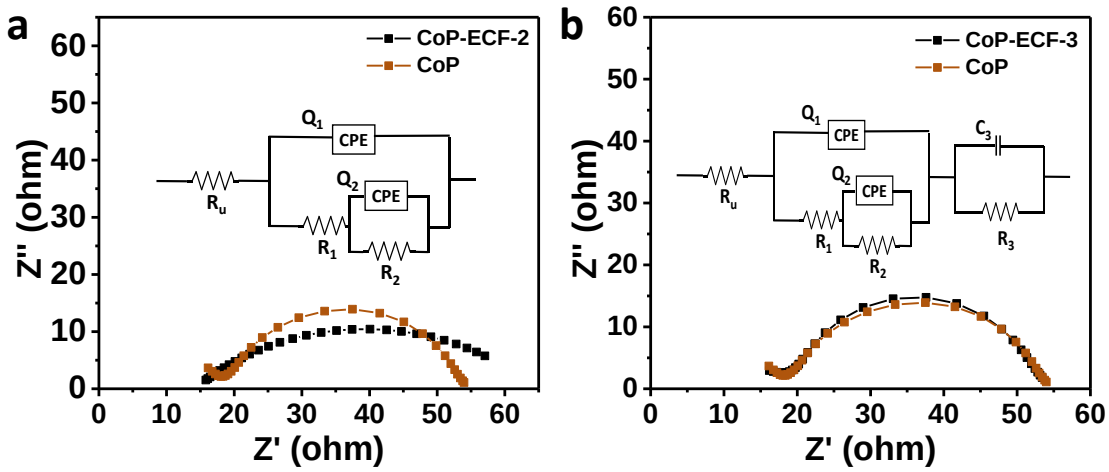

Fig. S15 (a,b) Electrochemical impedance Circuit fitting (ECF) of CoP catalyst.

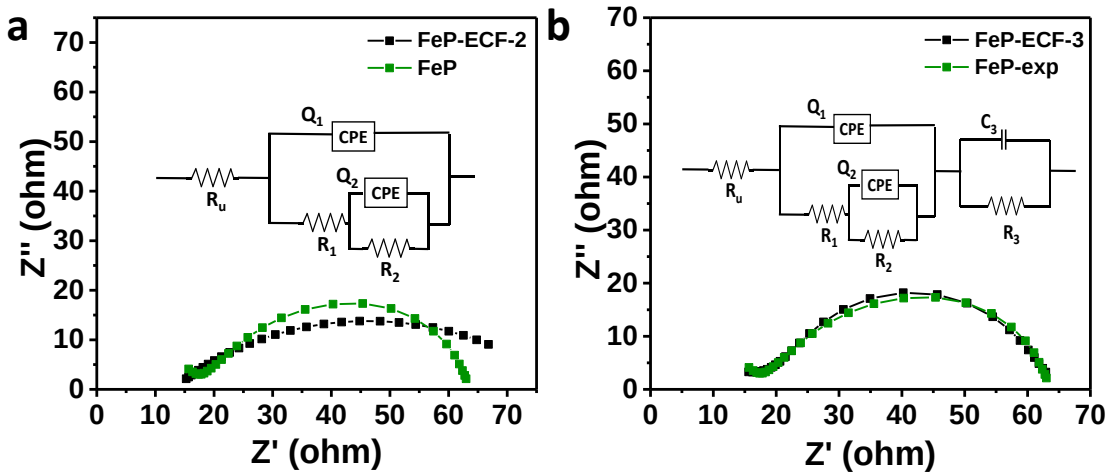

Fig. S16 (a,b) Electrochemical impedance Circuit fitting (ECF) of FeP catalyst.

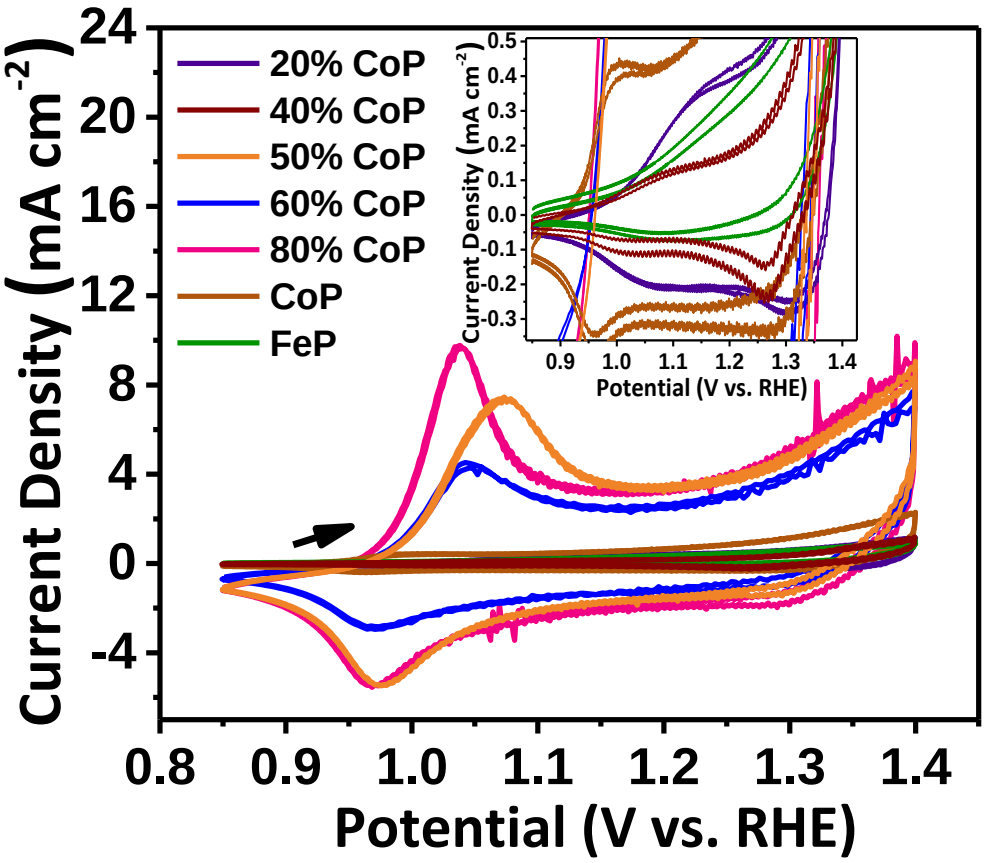

Fig. S17 Cyclic voltammograms (CV) of all catalysts with varying percentage of CoP in FeP.

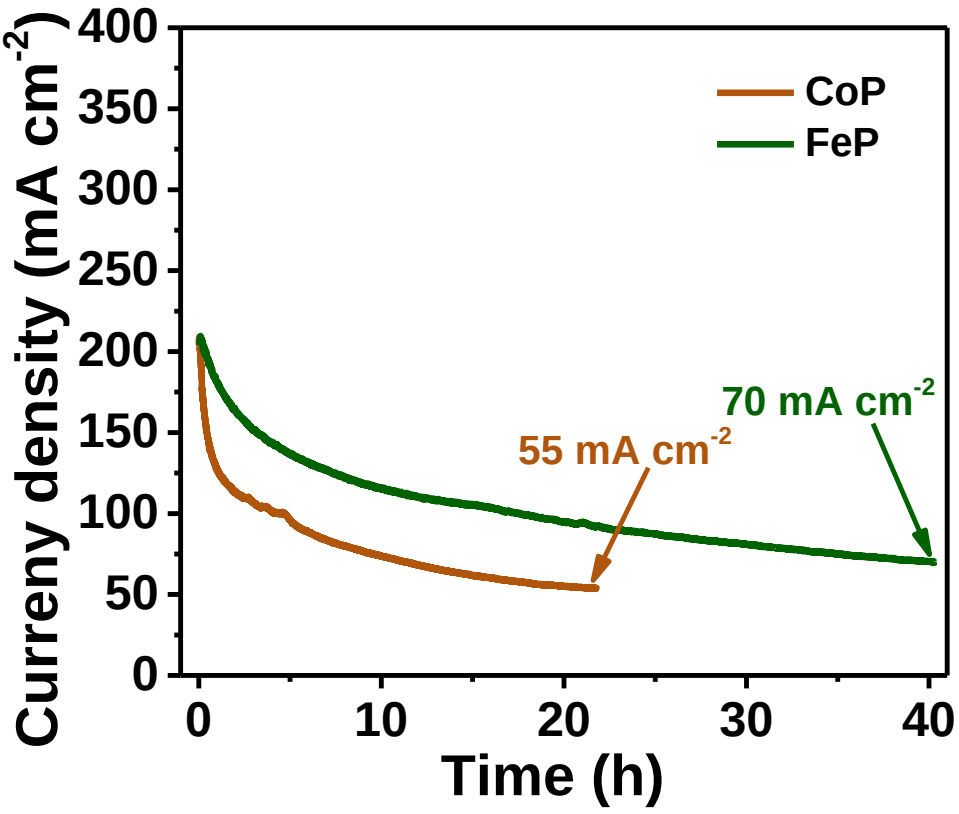

Fig. S18 Chronoamperometry study of individual FeP and CoP catalysts.

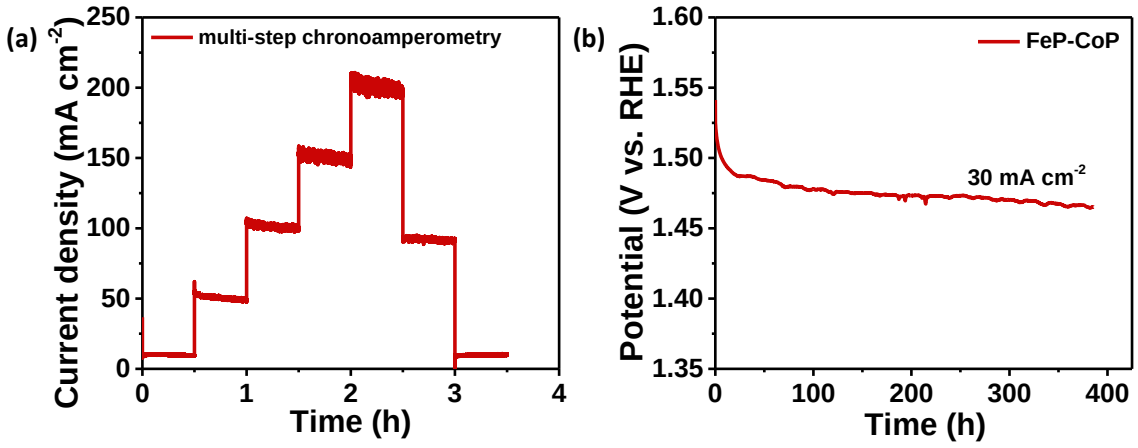

Fig. S19 (a) Multi step chronoamperometry study, and (b) galvanostatic study (to attain a low current density of 30 mA cm^{-2}) of (FeP-CoP) catalyst.

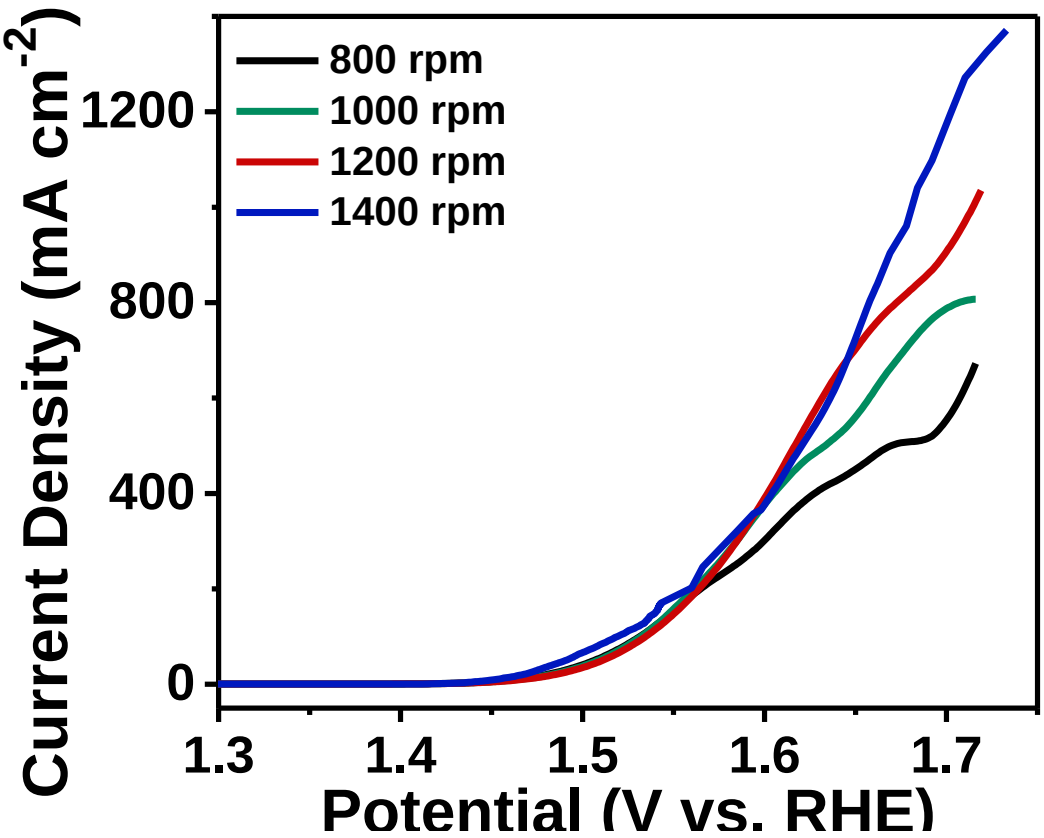

Fig. S20 Effect of stirring on electrocatalytic activity of (FeP-CoP) catalyst.

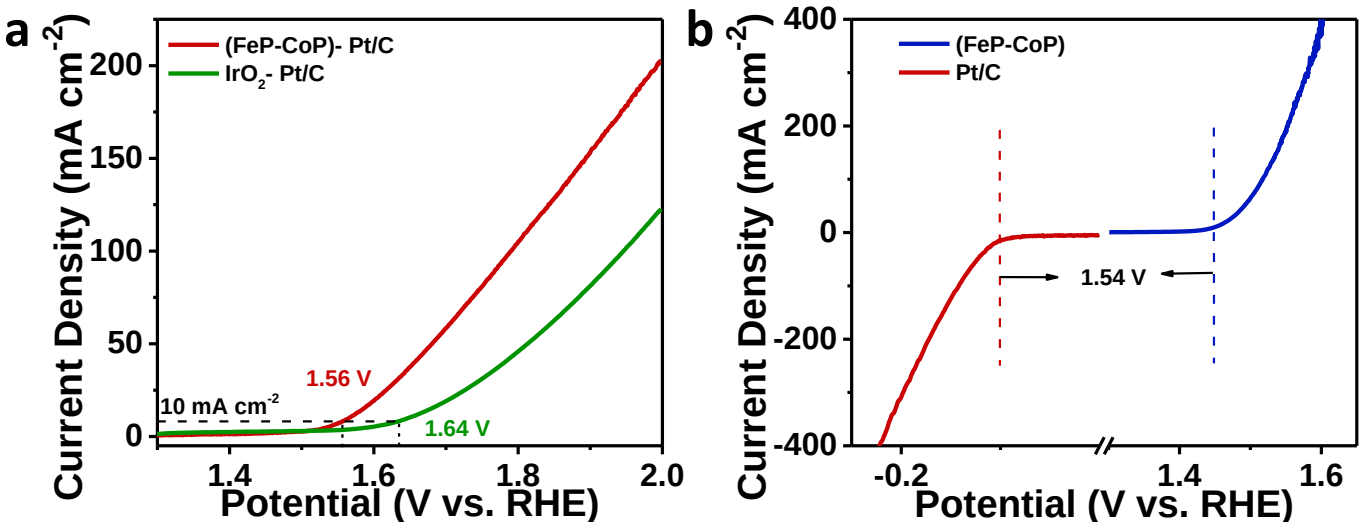

Fig. S21 (a) Full cell study in two-electrode arrangement employing (FeP-CoP) as the anode for OER and 20 -Pt/C as the cathode for HER in 1.0 M KOH, (b) half-cell LSVs of (FeP-CoP) and 20-Pt/C in 1. 0 M KOH.

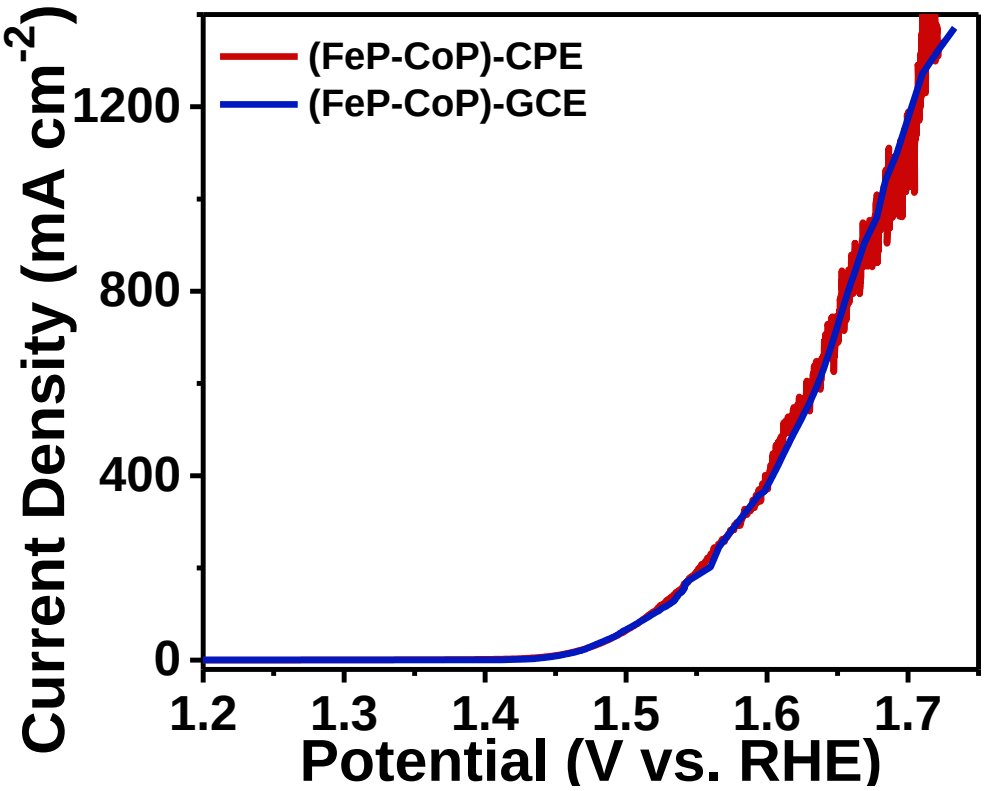

Fig. S22 Activity of (FeP-CoP) catalyst on GCE and CPE.

(GCE, and CPE are glassy carbon electrode and carbon paper electrode, respectively.)

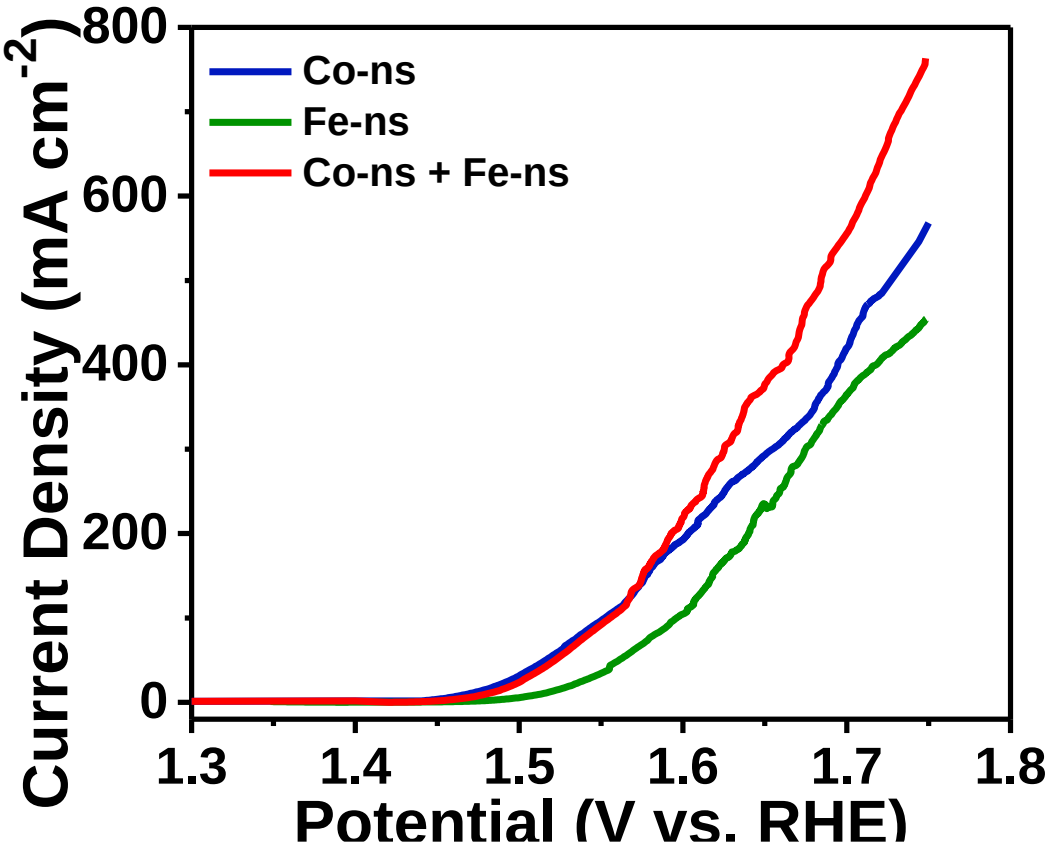

Fig. S23 Electrochemical activity of nano-sponges (ns) formed with $NaBH_4$ method.

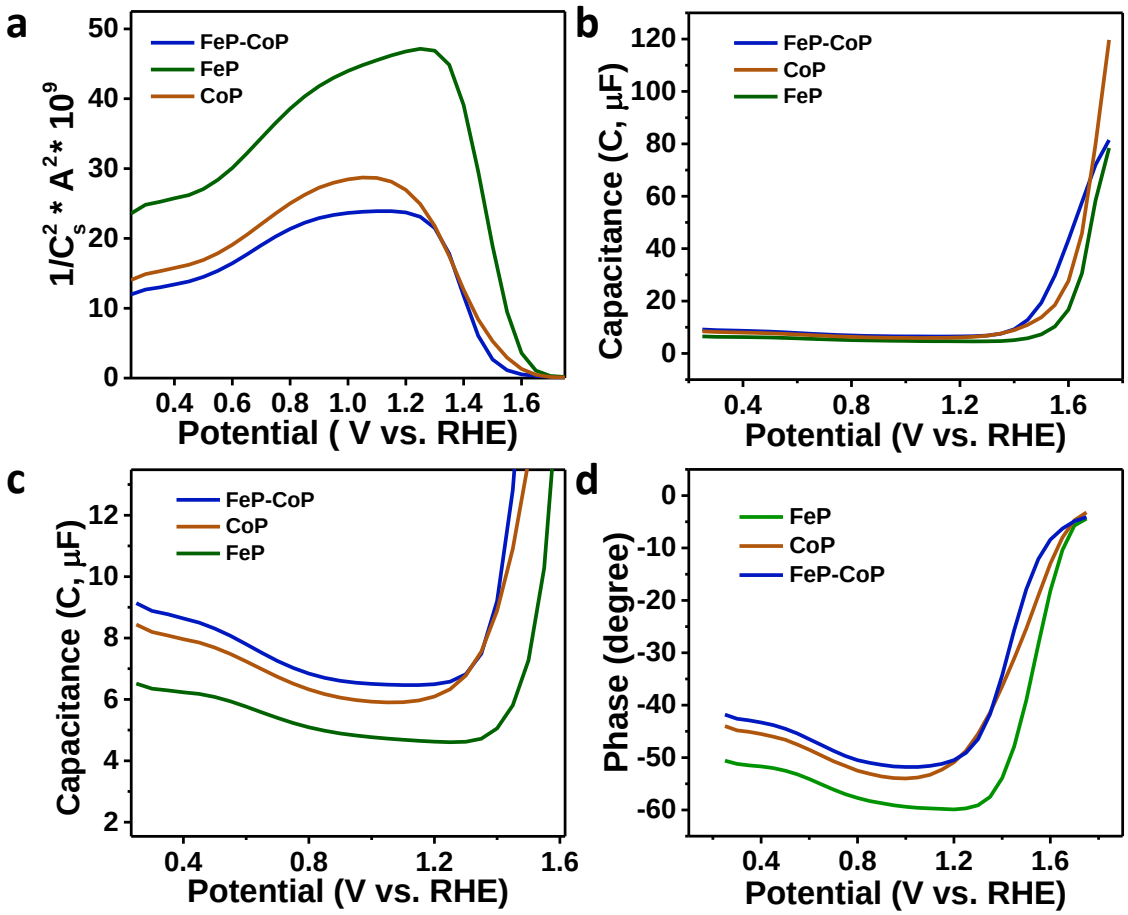

Fig. S24 Mott-Schottky study of various catalysts.

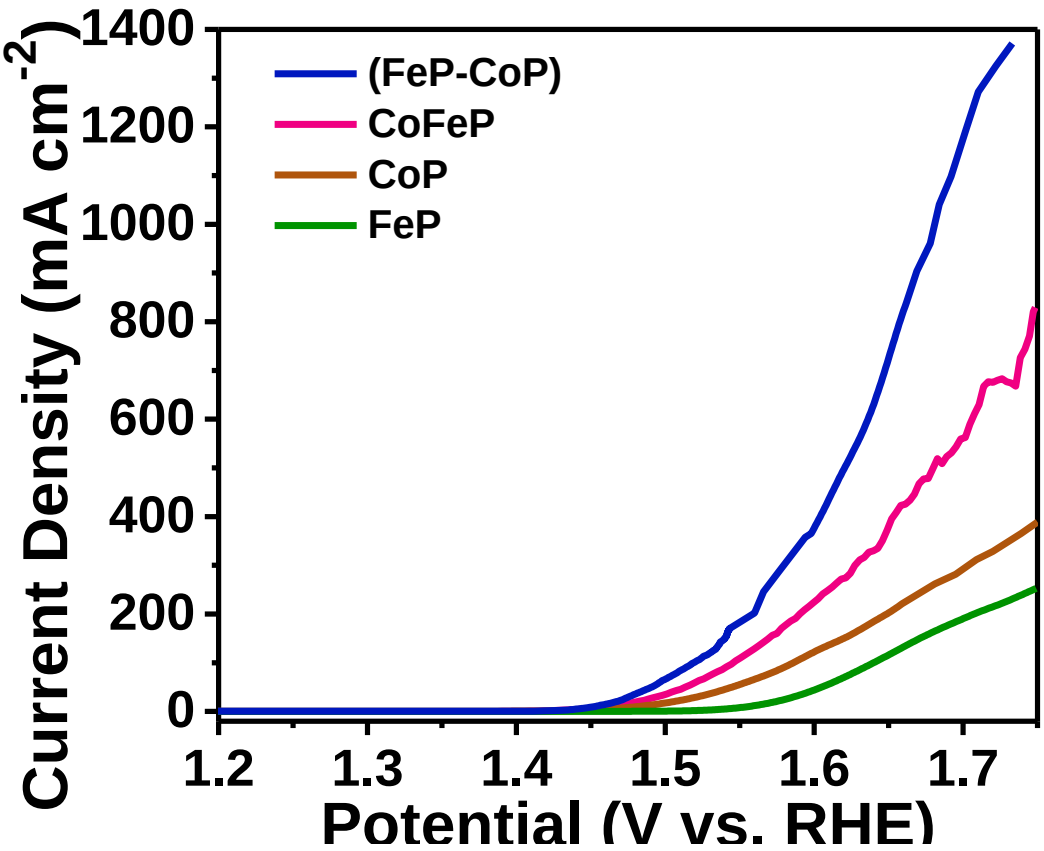

Fig. S25 Linear sweep voltammogram **(**LSV) of in-situ synthesized bimetallic (CoFeP) and other catalysts.

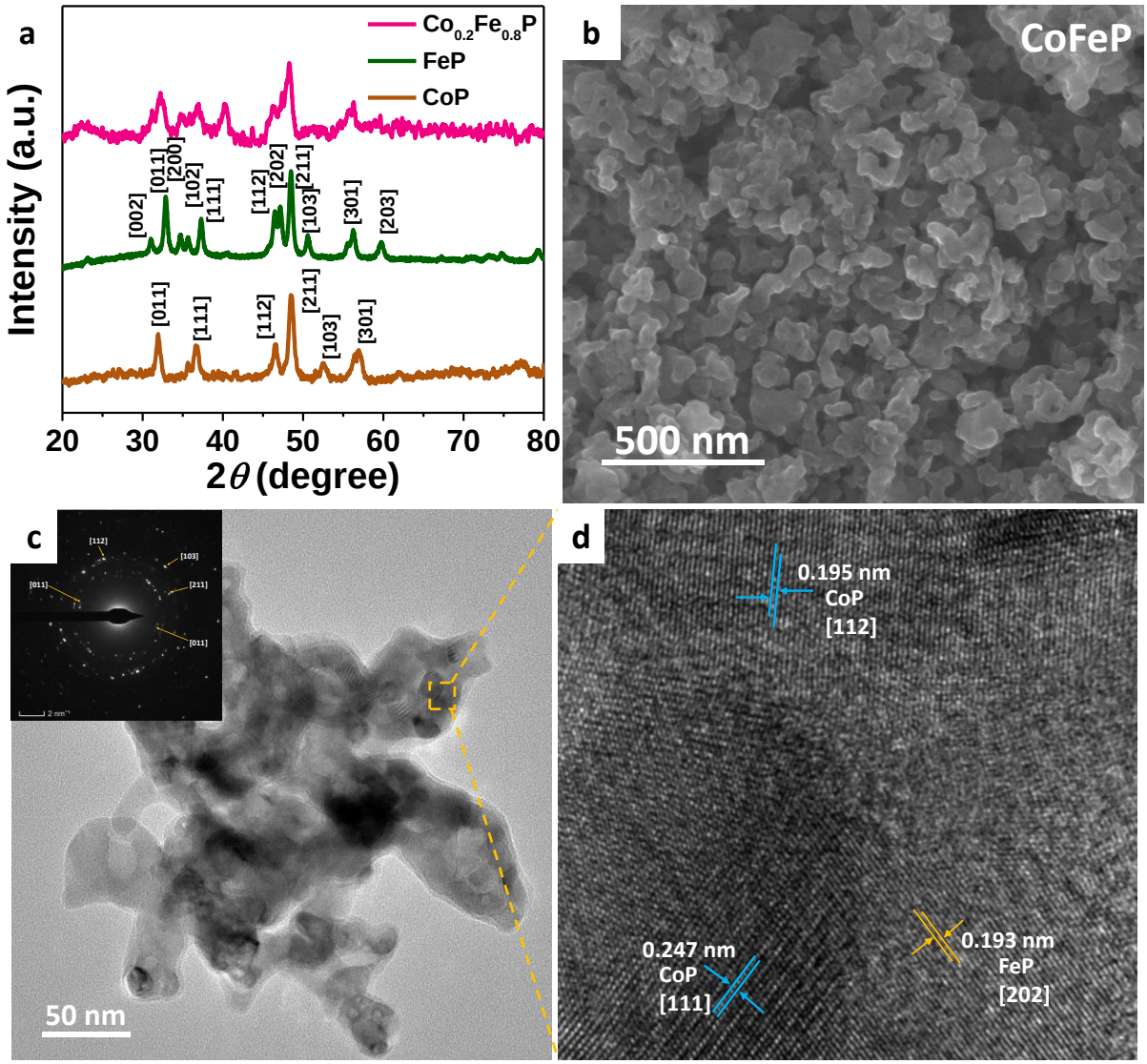

Fig. S26 (a) PXRD pattern, (b) FESEM, (c) TEM (inset shows SAED pattern), and (d) HRTEM of CoFeP catalyst.

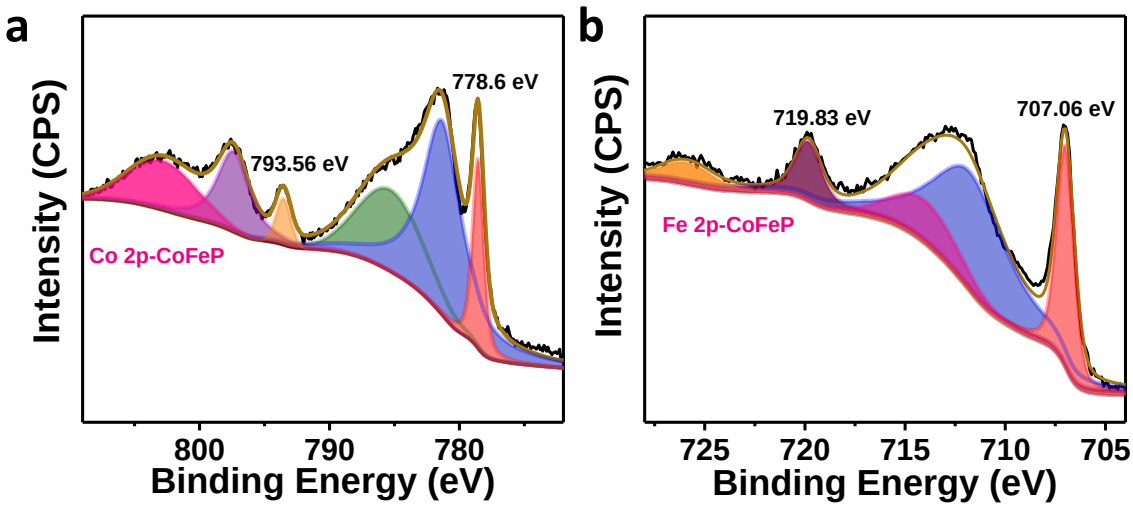

Fig. S27 High resolution XPS spectra of (a) Co 2p, and (b) Fe 2p of CoFeP catalyst.

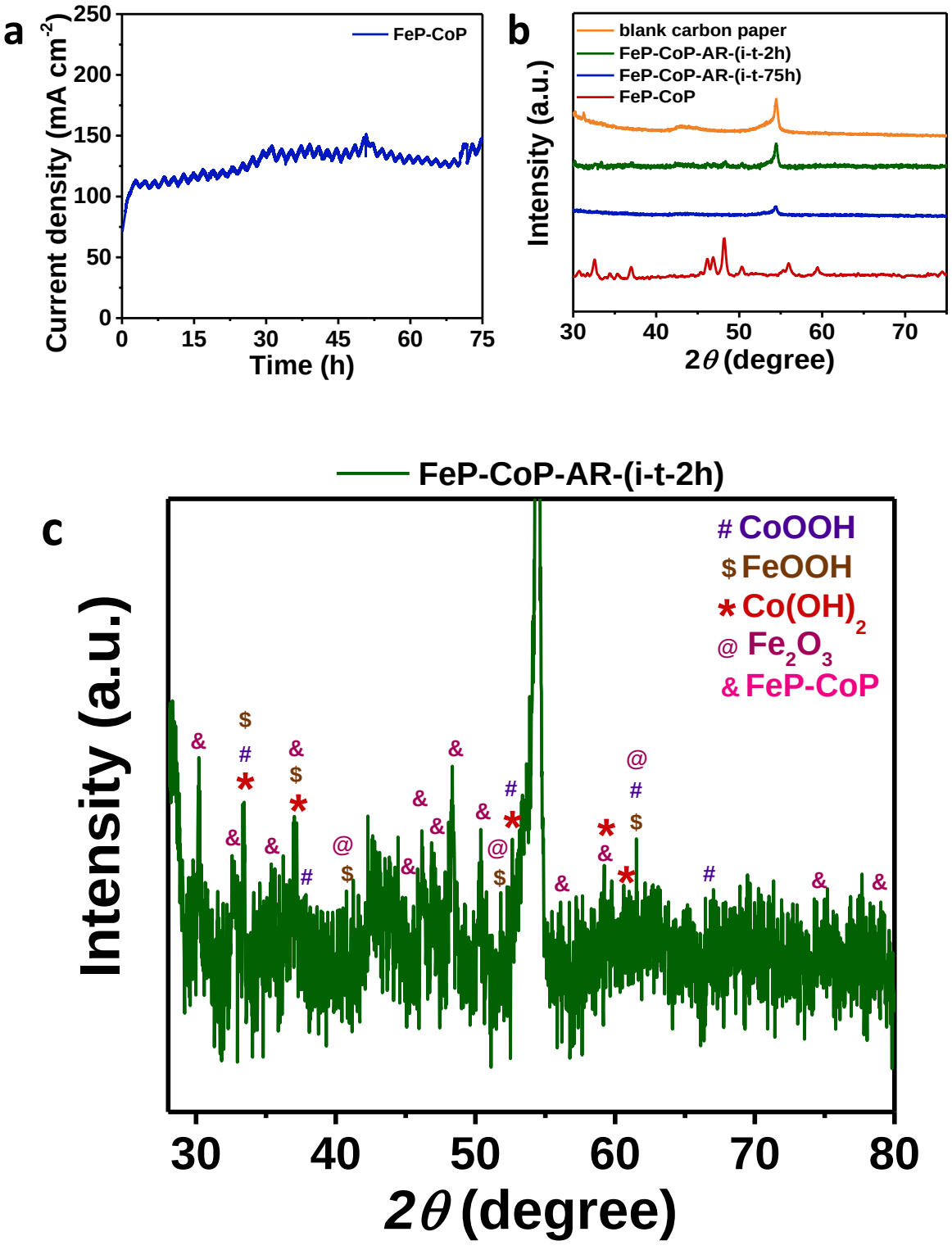
a
Current density (mA cm-2)
Time (h)
FeP-CoP
b
Intensity (a.u.)
2θ (degree)
blank carbon paper
FeP-CoP-AR-(i-t-2h)
FeP-CoP-AR-(i-t-75h)
FeP-CoP
c
FeP-CoP-AR-(i-t-2h)
Intensity (a.u.)
2θ (degree)
CoOOH
$ FeOOH
* Co(OH)2
@ Fe2O3
& FeP-CoP

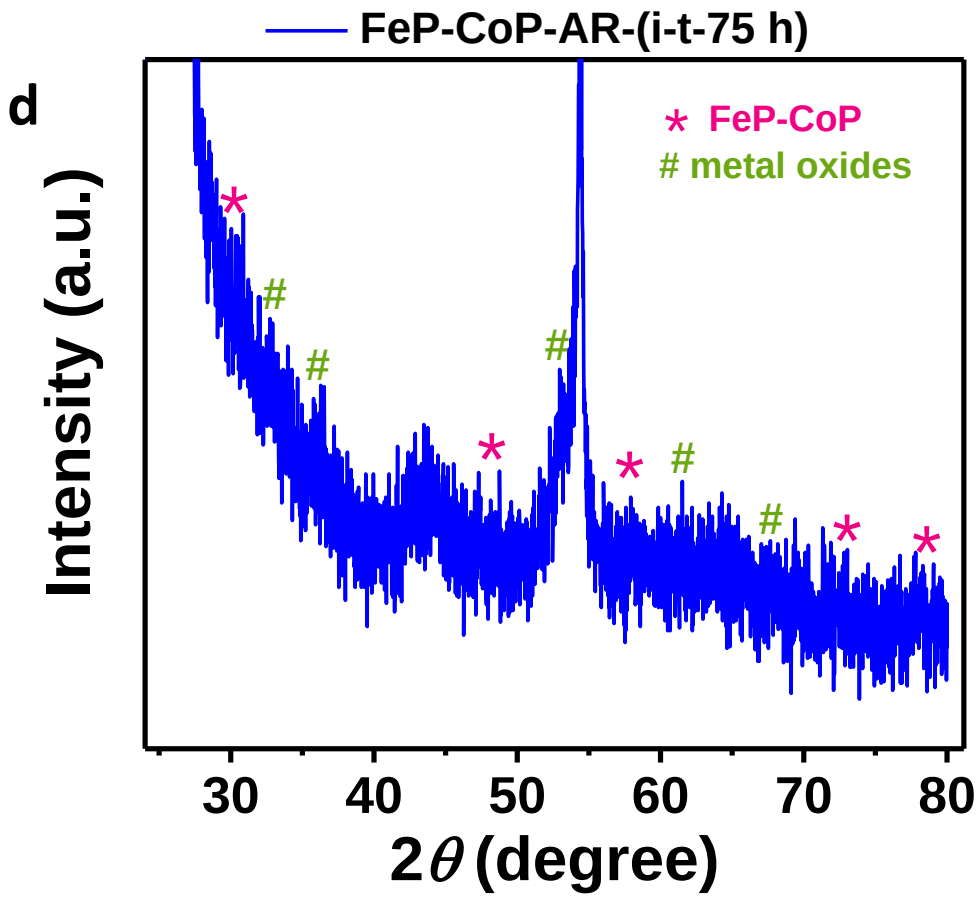

Fig. S28 (a) Chronoamperometry of FeP-CoP catalyst for 75 h, (b) PXRD pattern of FeP-CoP, blank carbon paper and FeP-CoP catalyst post OER (2 h, and 75 h), (c, d) PXRD pattern of FeP-CoP post OER for 2 h, and 75 h, respectively.

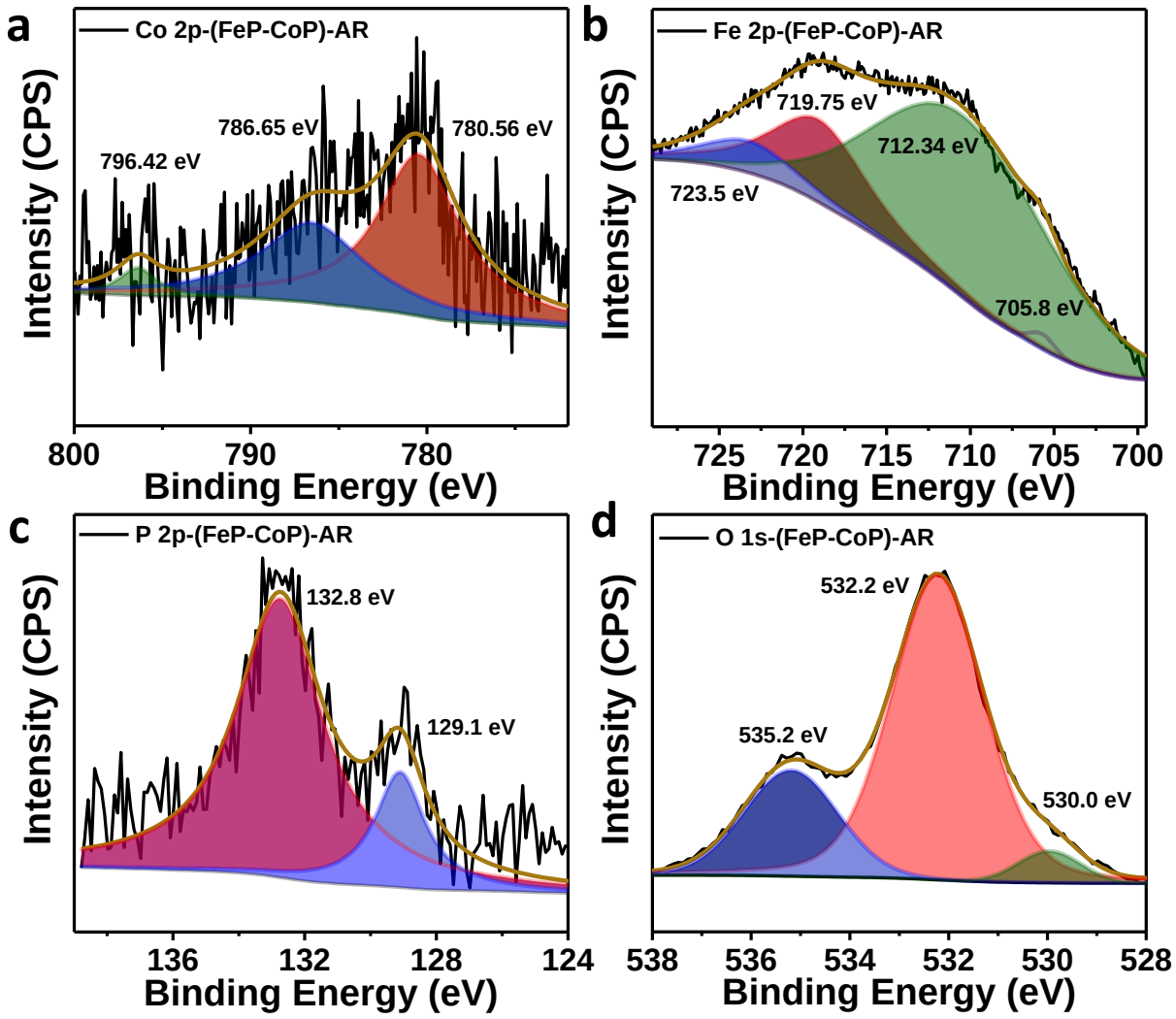

Fig. S29 High resolution XPS spectra of (a) Co 2p, (b) Fe 2p, (c) P 2p, and (d) O 1s for (FeP-CoP) catalyst post OER for 2 h.

(AR means “after reaction”)

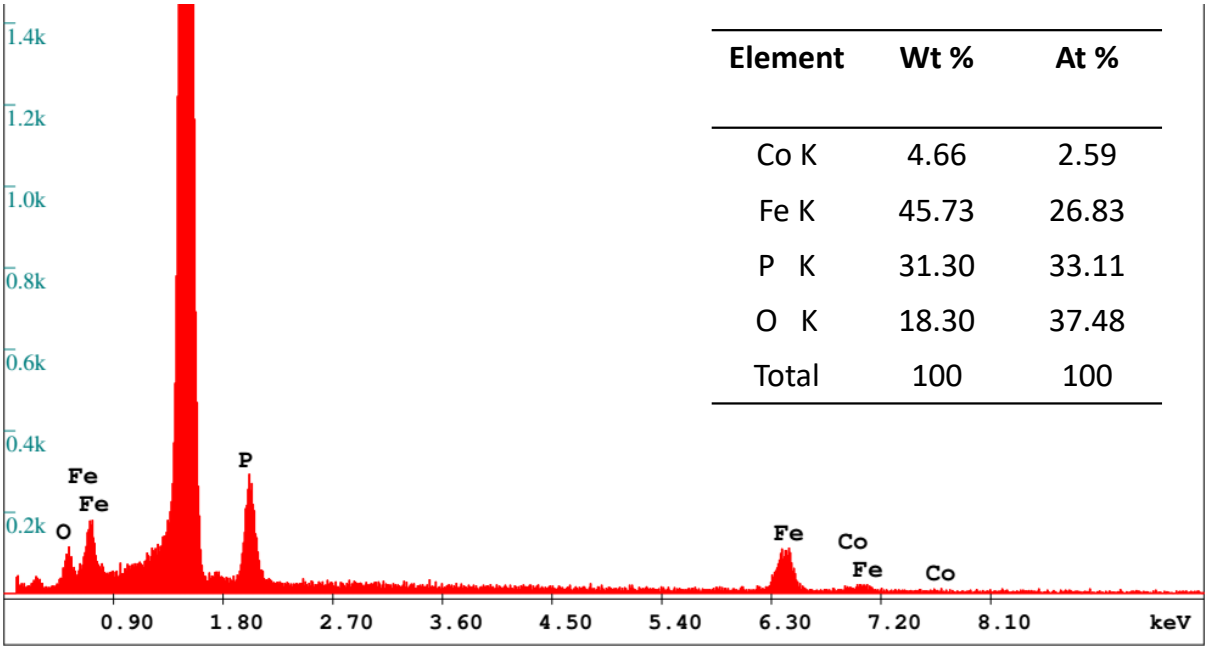

Element	Wt %	At %
Co K	4.66	2.59
Fe K	45.73	26.83
P K	31.30	33.11
O K	18.30	37.48
Total	100	100

Fig. S30 EDS elemental plot of FeP-CoP catalyst post OER after 2 h.

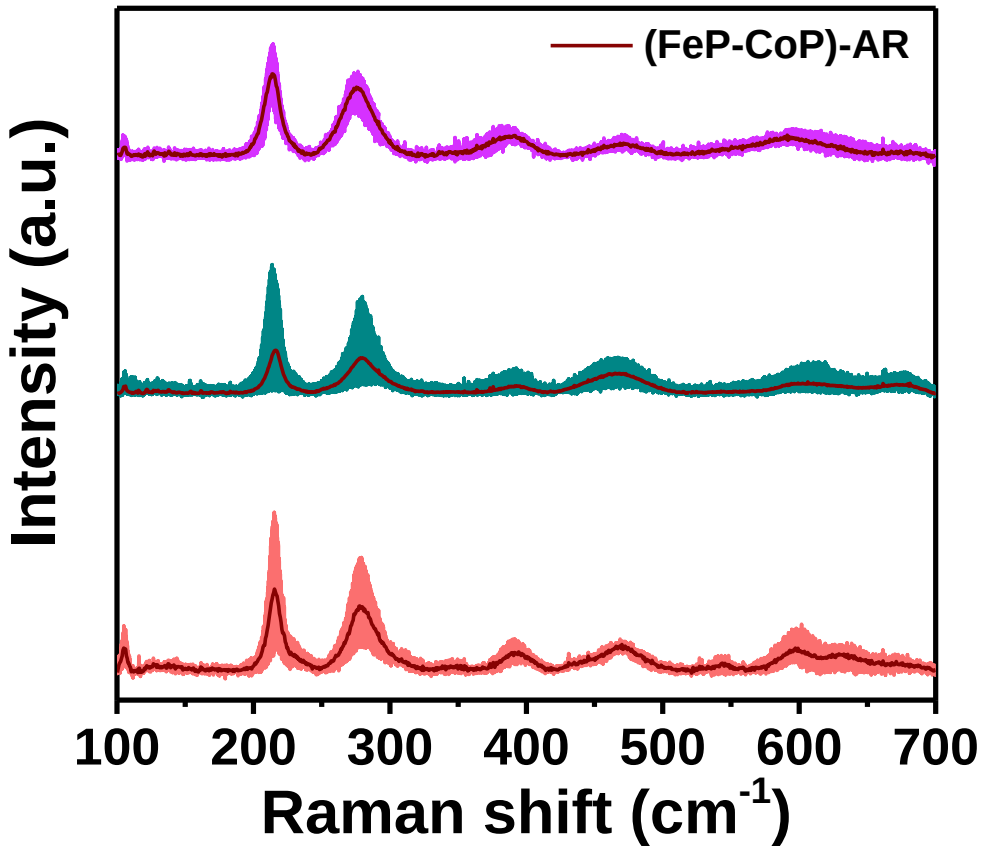

Fig. S31 Raman spectra of (FeP-CoP) catalyst post OER for 2 h. (AR means after reaction).

The three spectra represent the spatial variations of the Raman spectra over the 90 points in the FeP-CoP sample post OER.

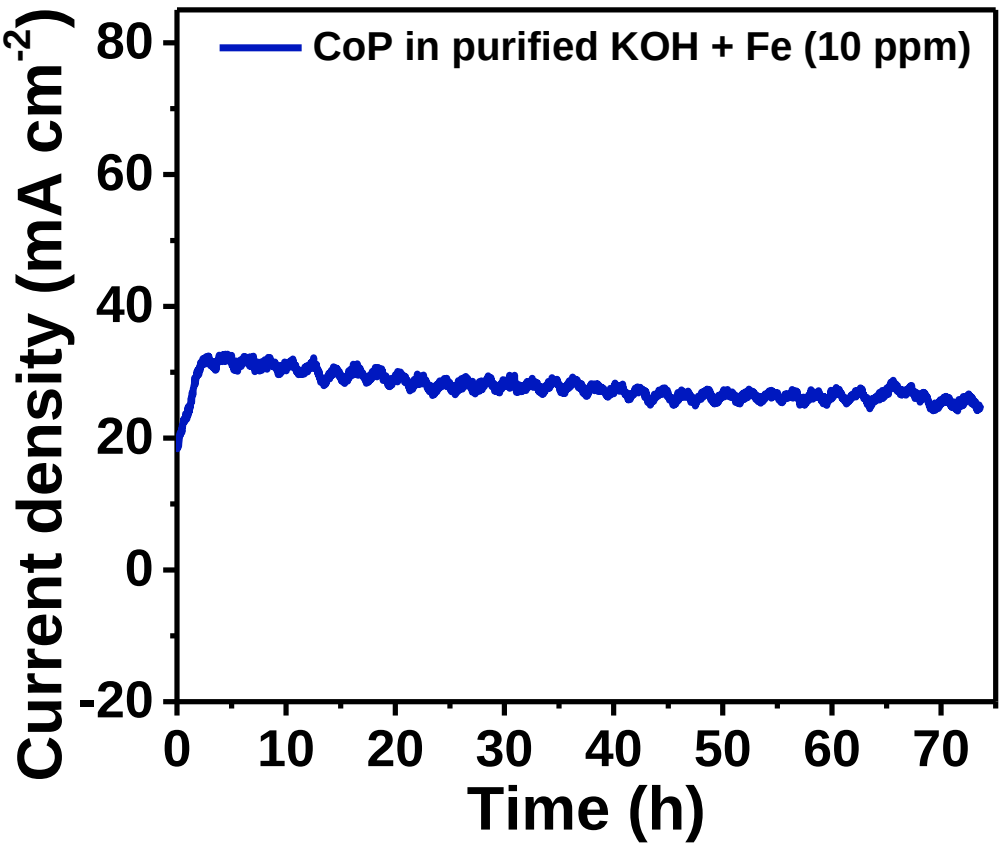

Fig. S32 Chronometry of CoP in presence of Fe (10 ppm) in 1 M purified KOH.

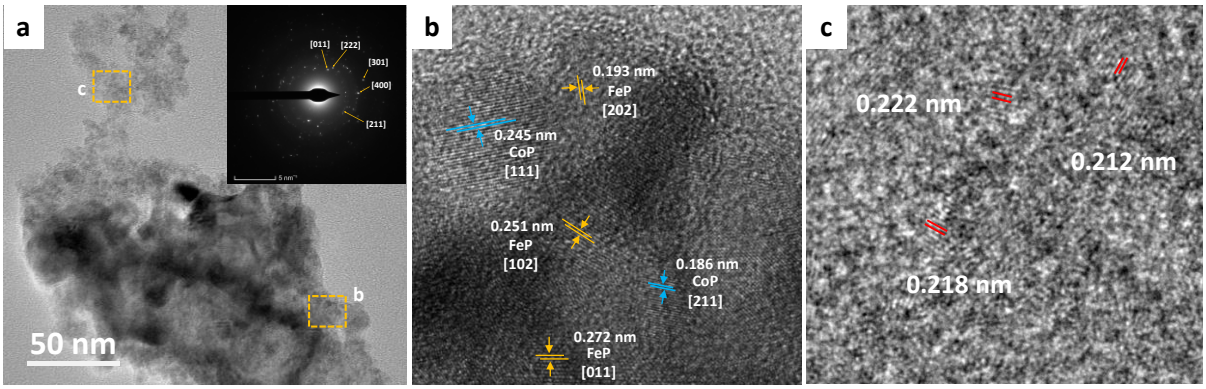

Fig. S33 (a) TEM (inset shows SAED pattern), and (b, c) HRTEM of (FeP-CoP) catalyst post OER for 2 h.

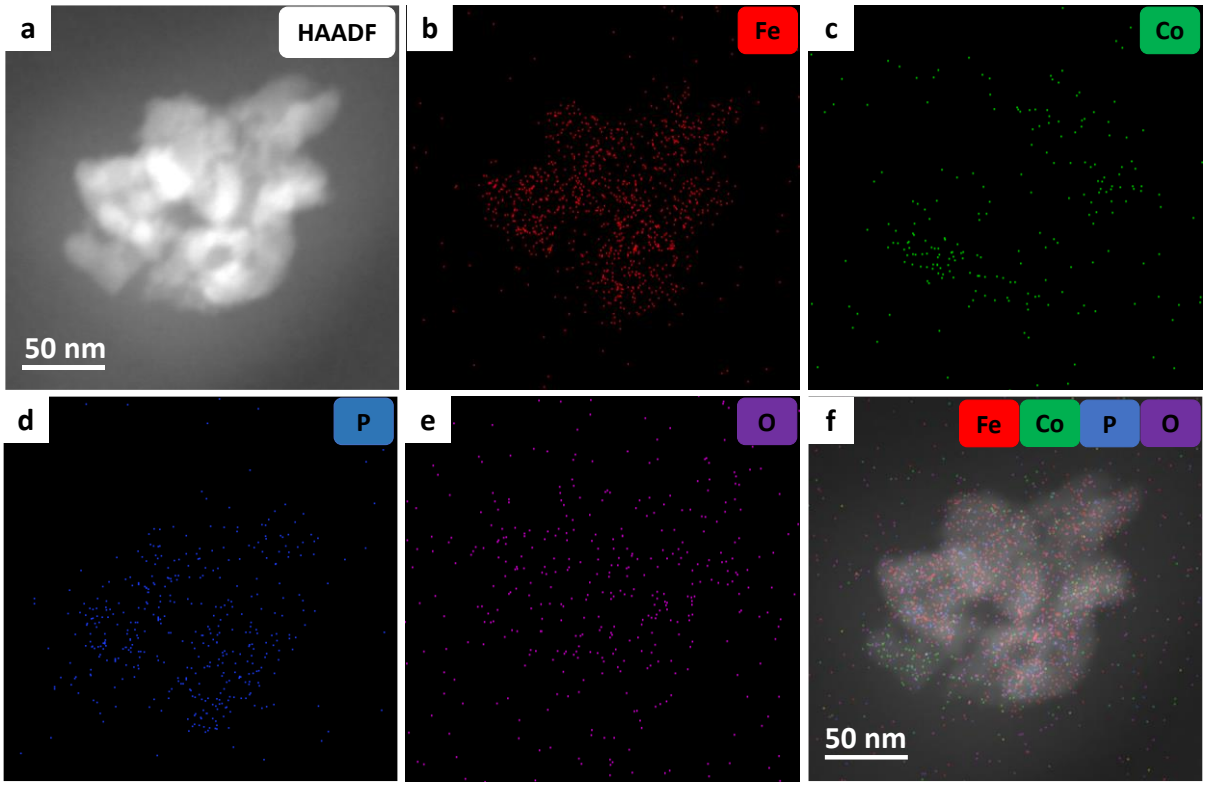

Fig. S34 (a) HAADF, (b) Fe, (c) Co, (d) P, (e) O, and (f) all elements mapping of (FeP-CoP) catalyst post OER for 2 h in HAADF-STEM mode.

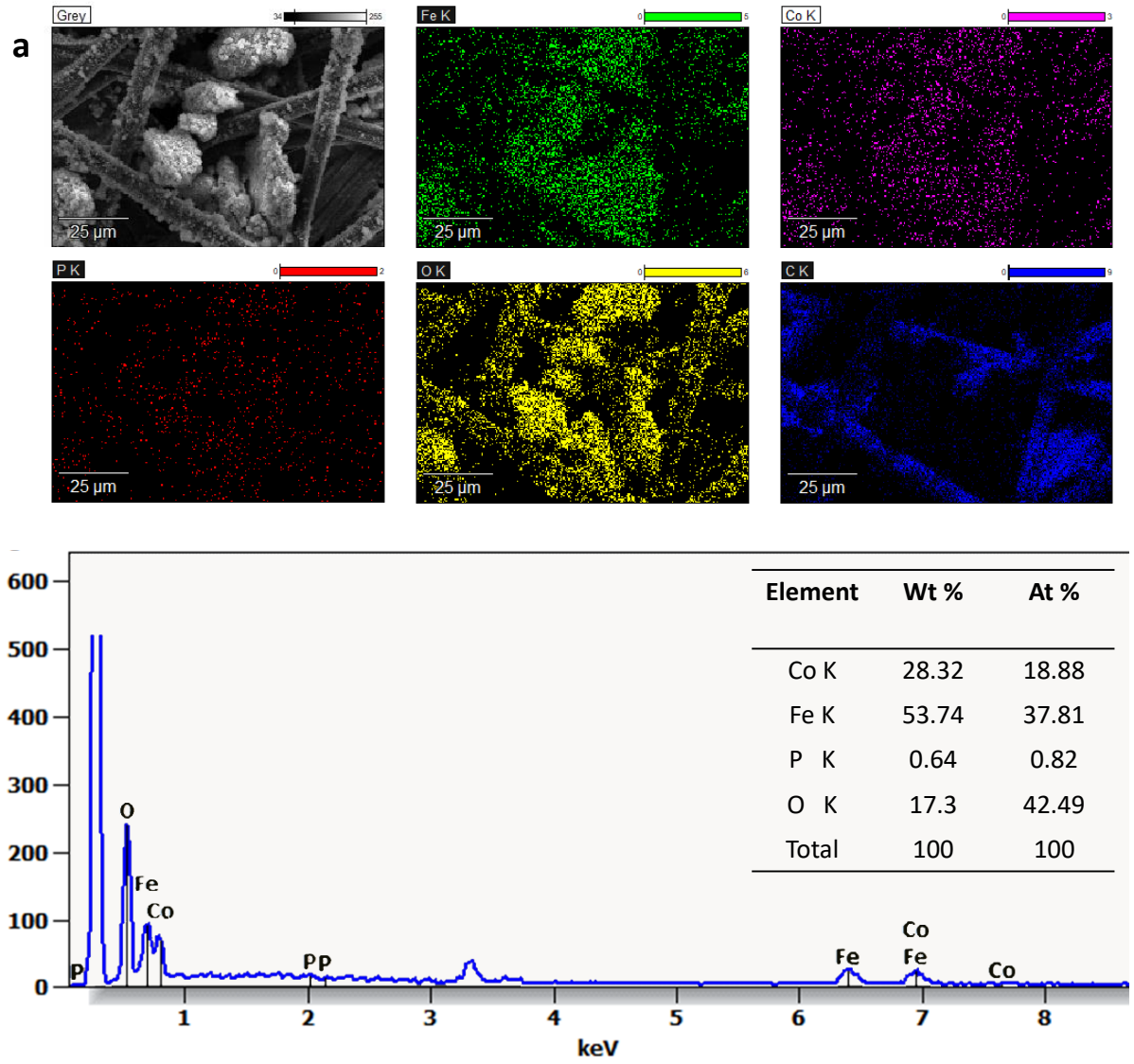

Element	Wt %	At %
Co K	28.32	18.88
Fe K	53.74	37.81
P K	0.64	0.82
O K	17.3	42.49
Total	100	100

Fig. S35 EDS elemental mapping and plot of FeP-CoP catalyst post OER after 75 h.

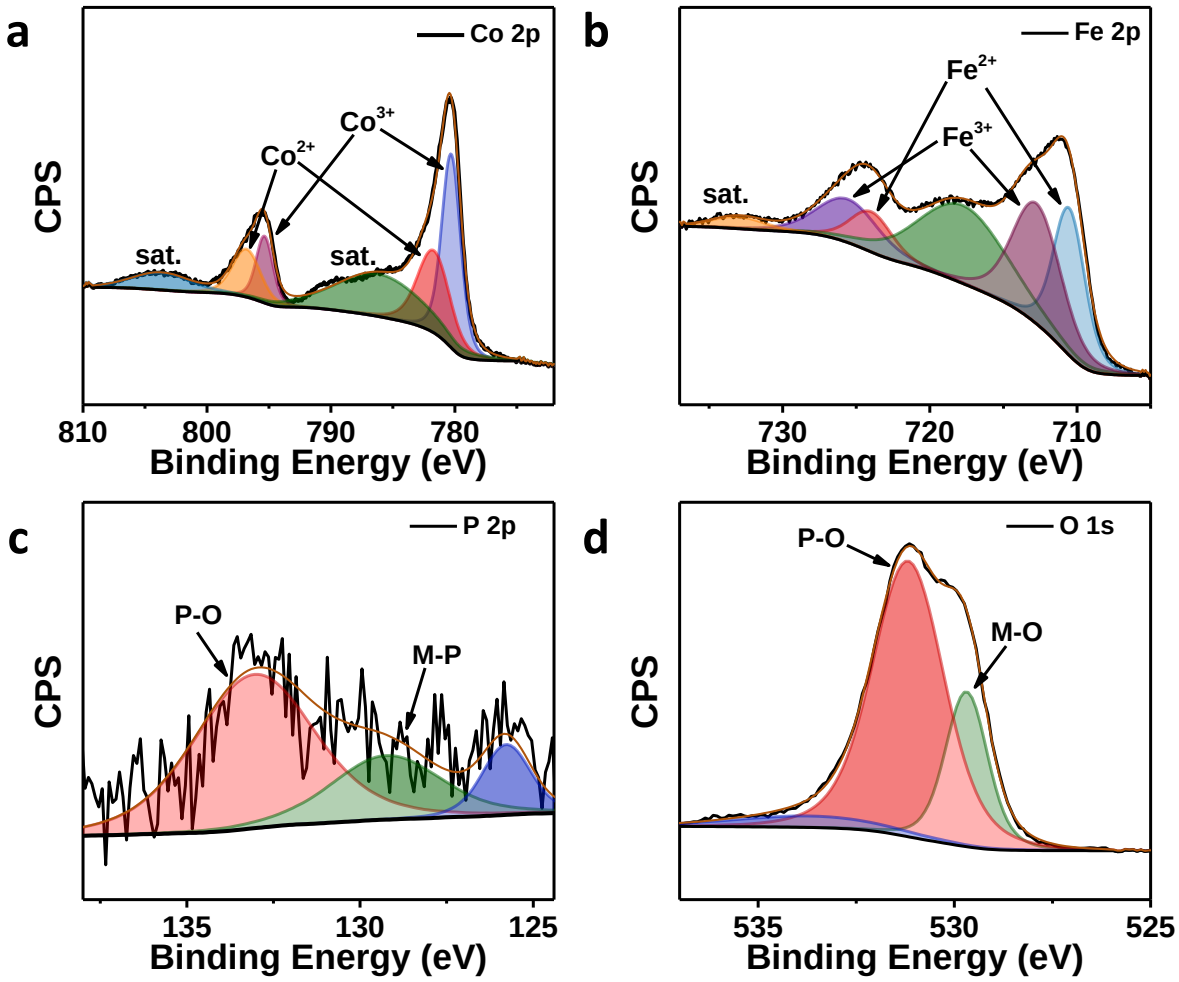

Fig. S36 High resolution XPS spectra of (a) Co 2p, (b) Fe 2p, (c) P 2p, and (d) O 1s for (FeP-CoP) catalyst post OER for 75 h.

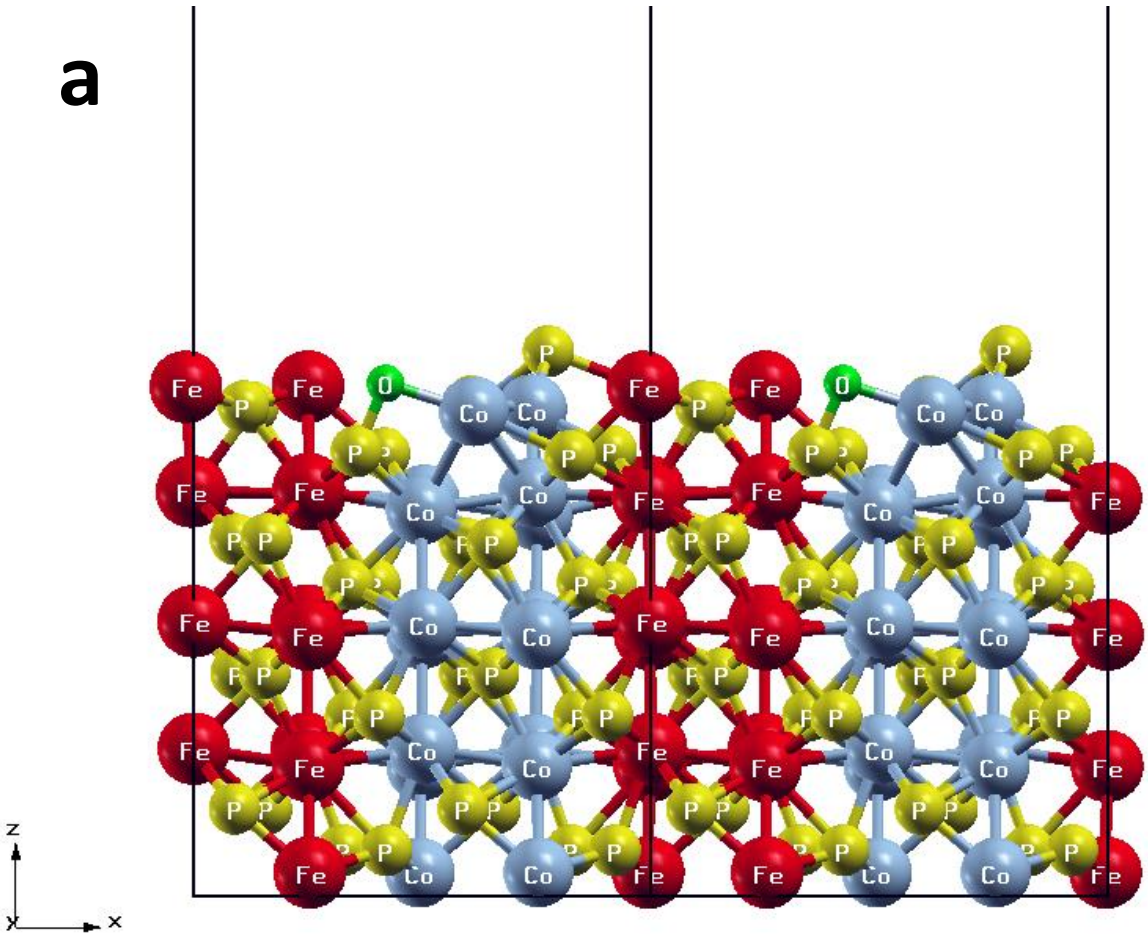
a
Fe
P
O
Co
z
x
y

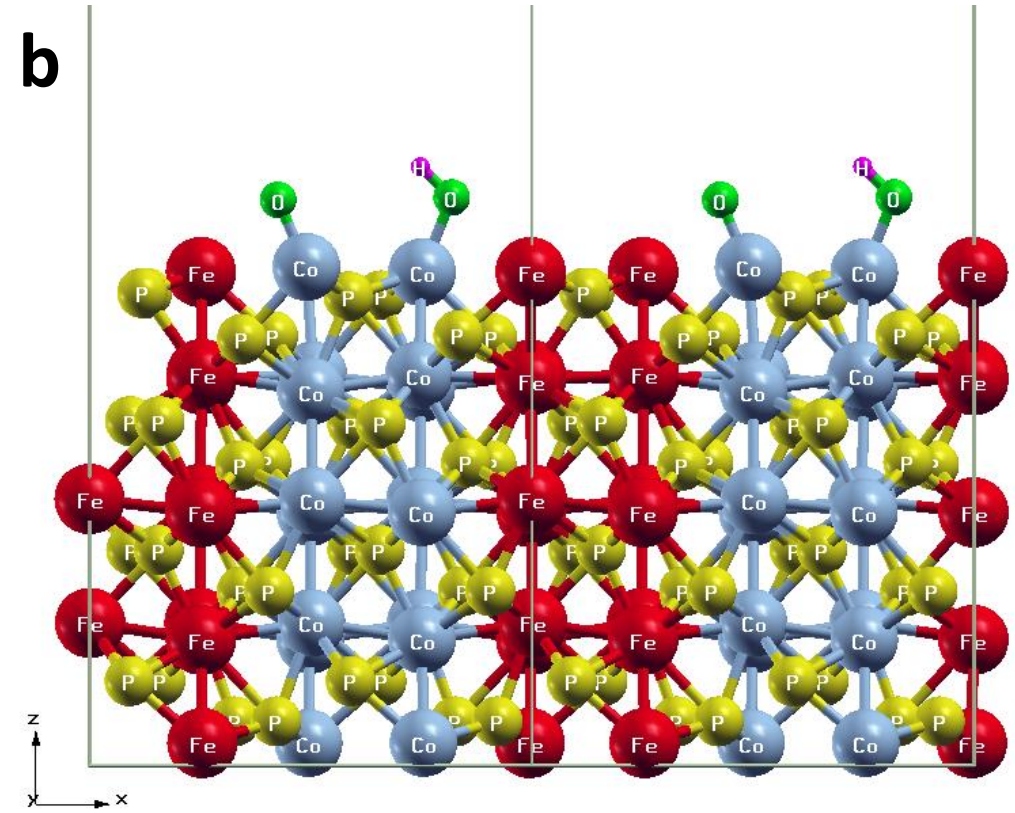
b
H
O
Co
Fe
P
z
x

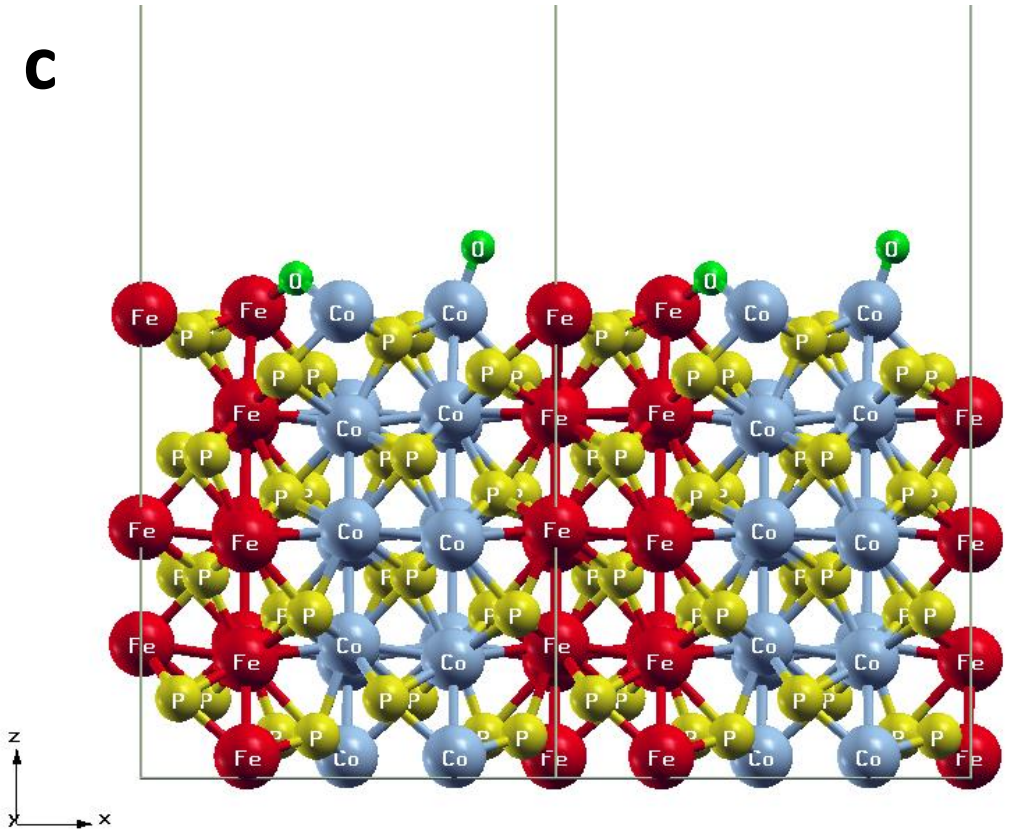
c
O
Co
Fe
P
z
x

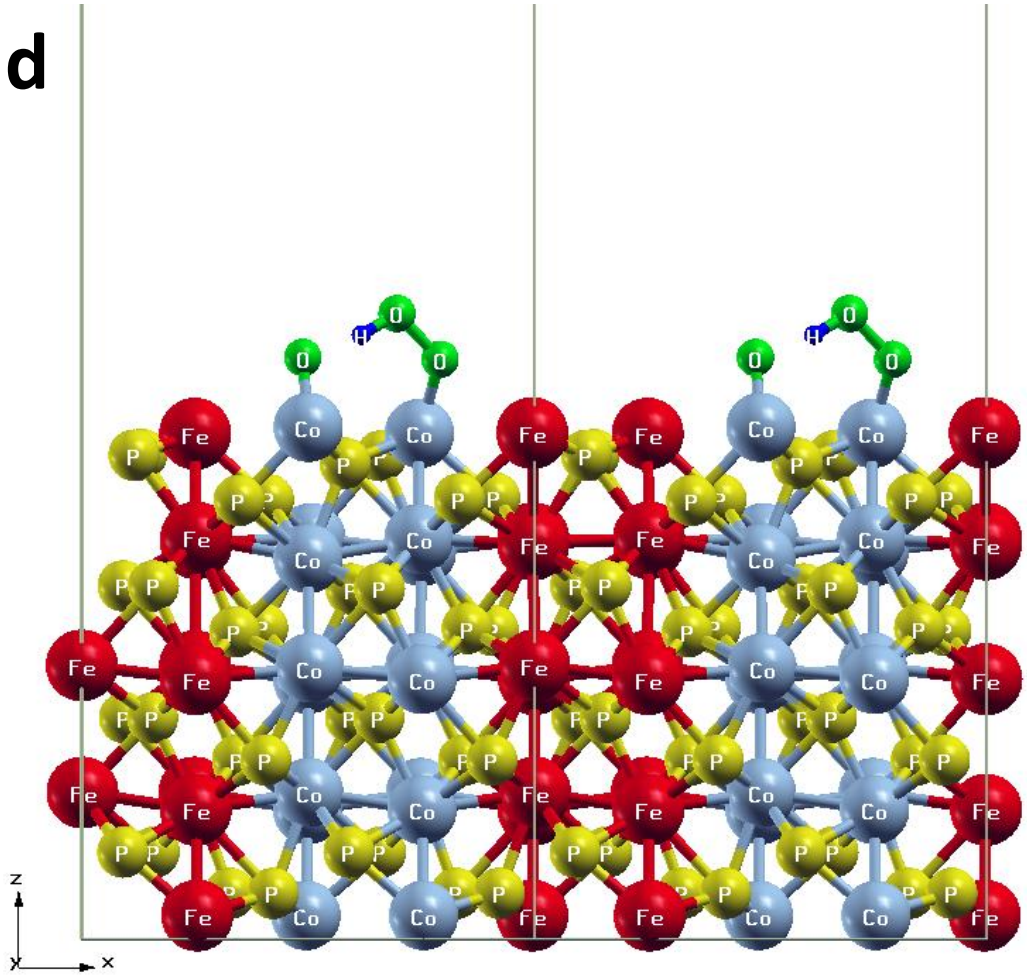

Fig. S37 Stable configurations of various intermediates on FeP-CoP interface with one surface oxygen atom.

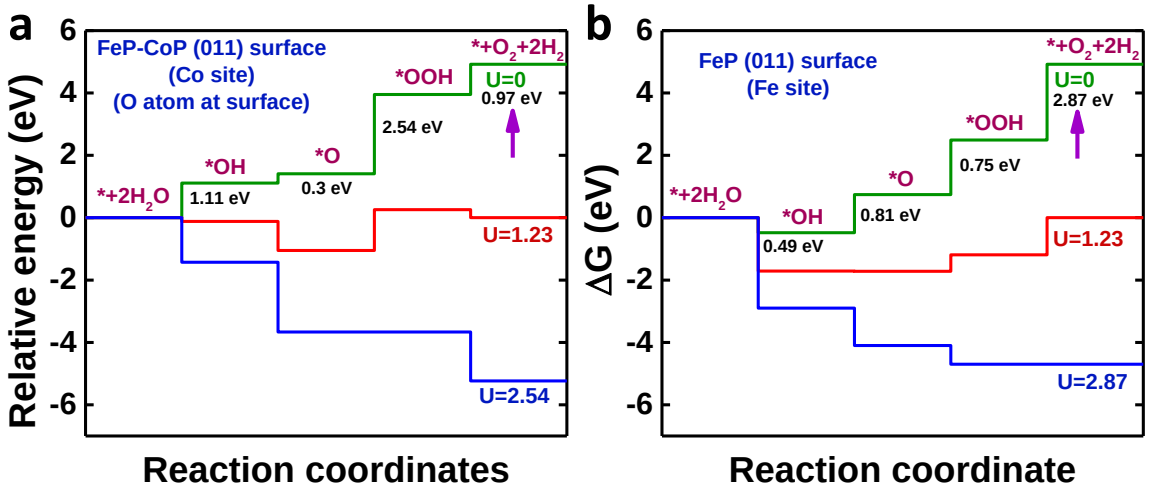

Fig. S38 Relative energy for each step in OER mechanism for (a) FeP-CoP interface with one surface oxygen atom, (b) FeP surface with Fe as the adsorption site.

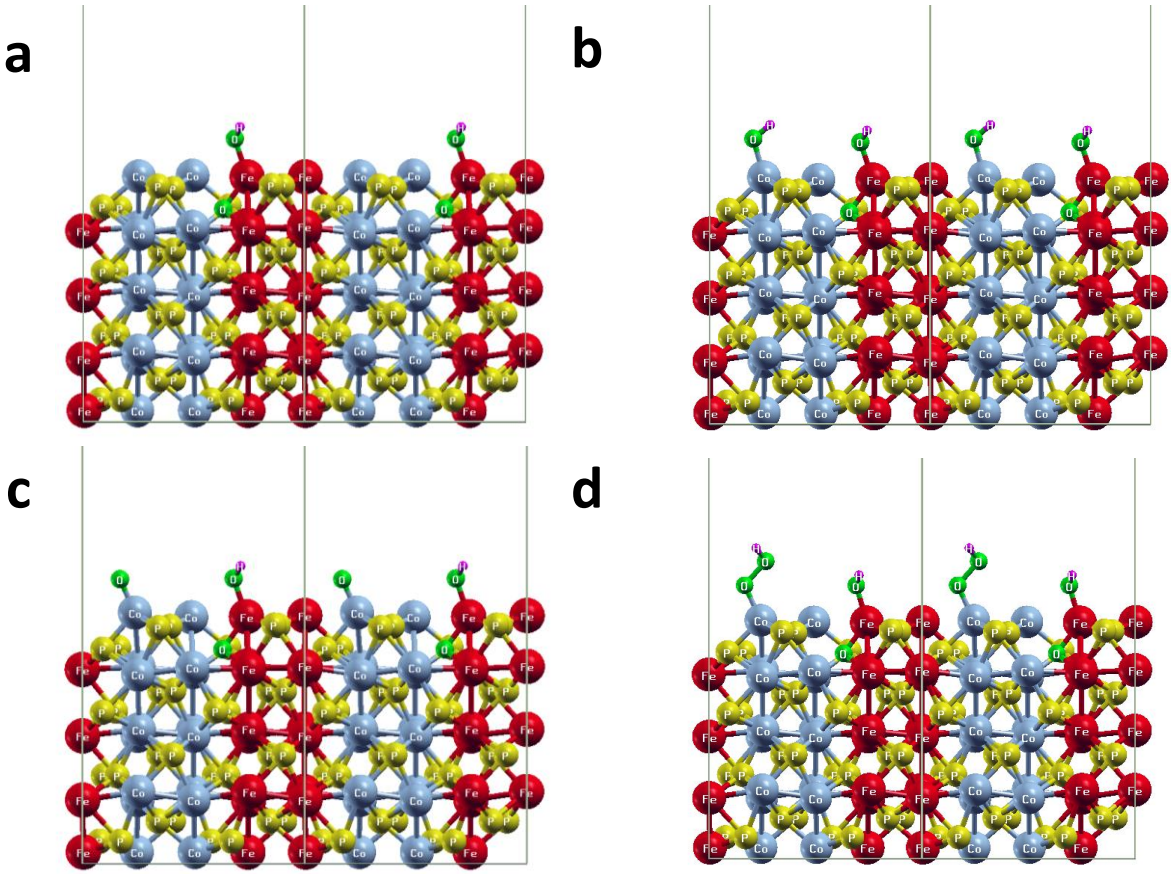

Fig. S39 Stable configurations of (a) FeOOH structure, (b-d) various intermediates considering FeOOH on the surface of FeP-CoP interface with Co as the intermediate adsorption site.

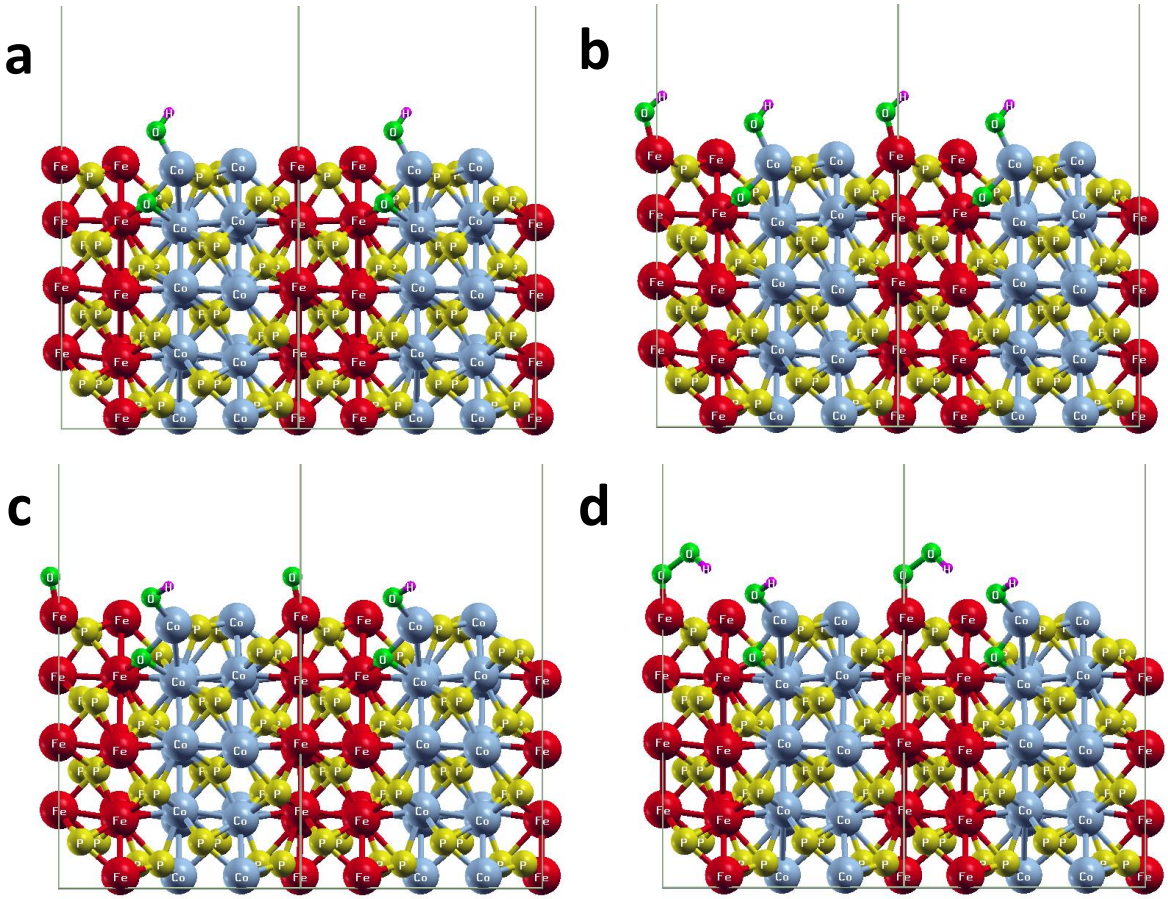

Fig. S40 Stable configurations of (a) CoOOH structure, (b-d) various intermediates considering CoOOH on the surface of FeP-CoP interface with Fe as the intermediate adsorption site.

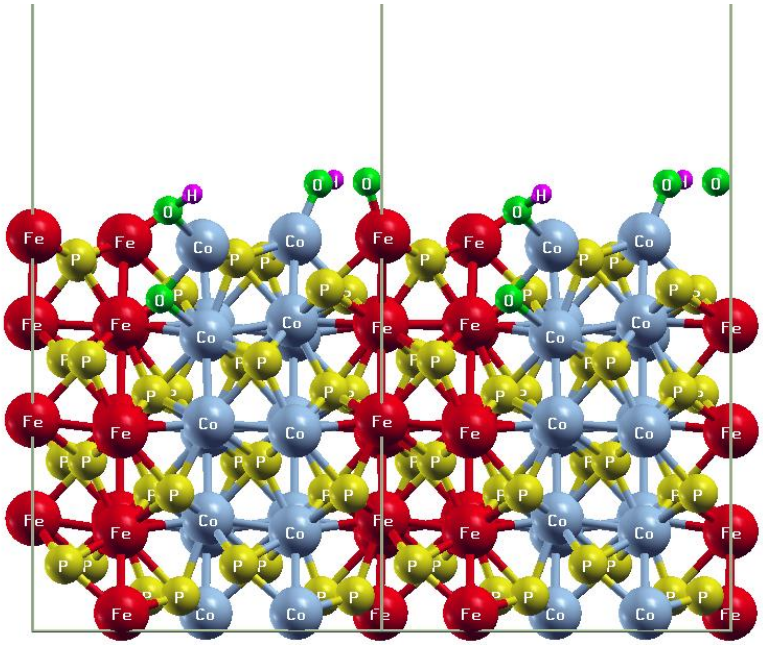

Fig. S41 Unstable configuration of adsorption of OOH intermediate on Co site considering CoOOH on the surface of FeP-CoP interface.

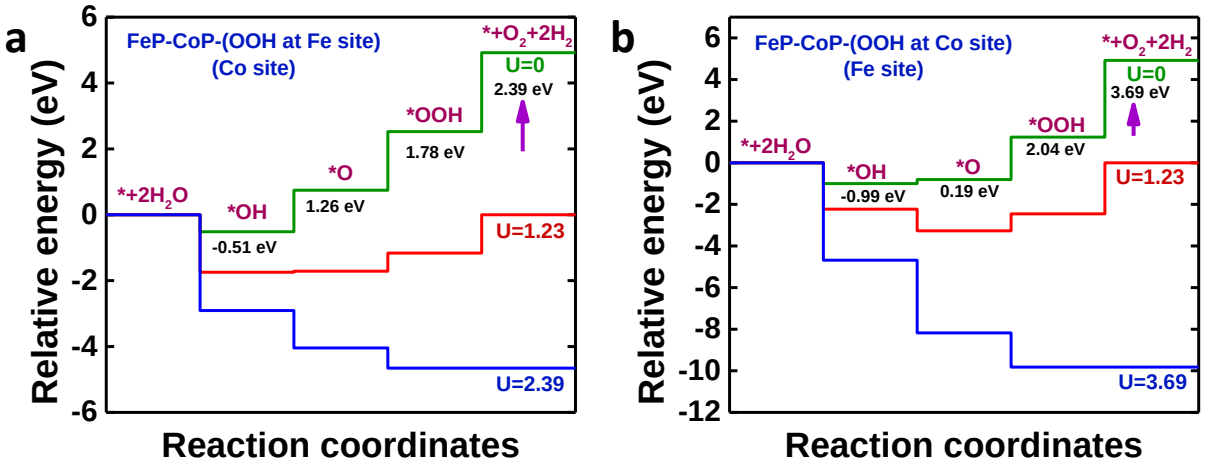

Fig. S42 Relative energy for each step in OER mechanism for (a) FeOOH at surface of FeP-CoP interface with Co as intermediate adsorption site, and (b) CoOOH at surface of FeP-CoP interface with Fe as intermediate adsorption site.

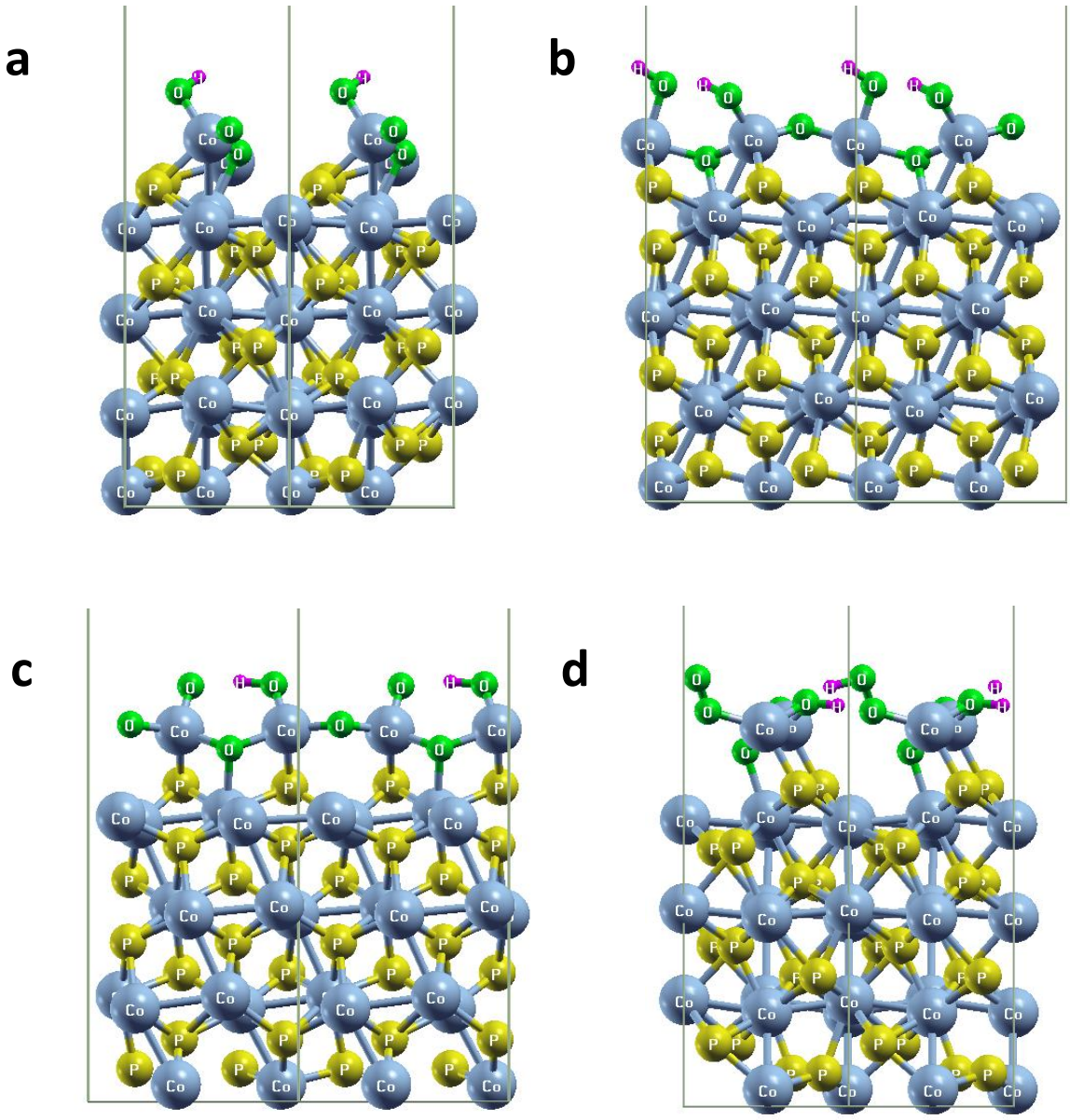

Fig. S43 Stable configurations of (a) surface, (b-d) and various intermediates (*OH, *O, *OOH) considering oxygenated surface on CoP catalyst.

a

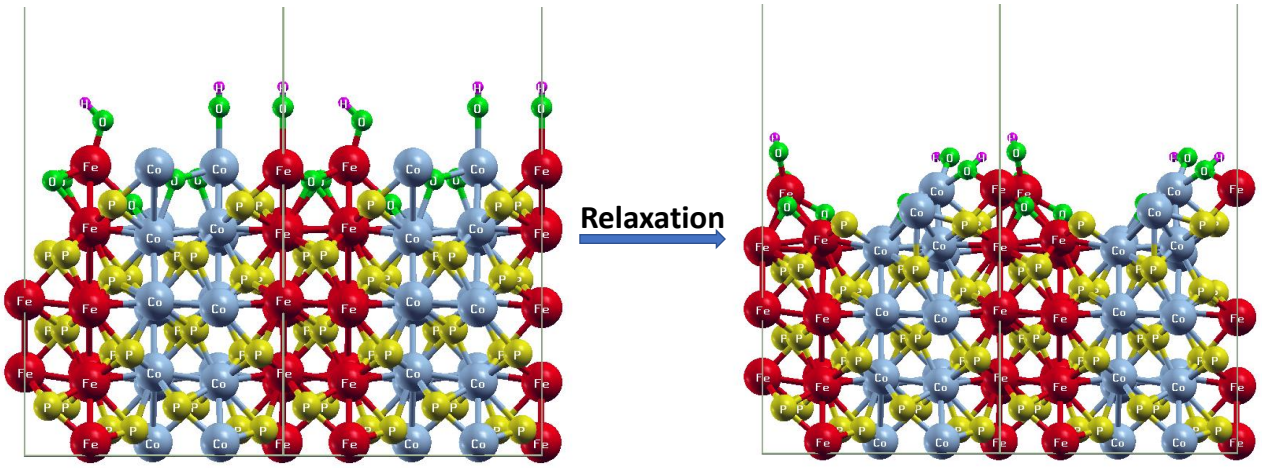

b

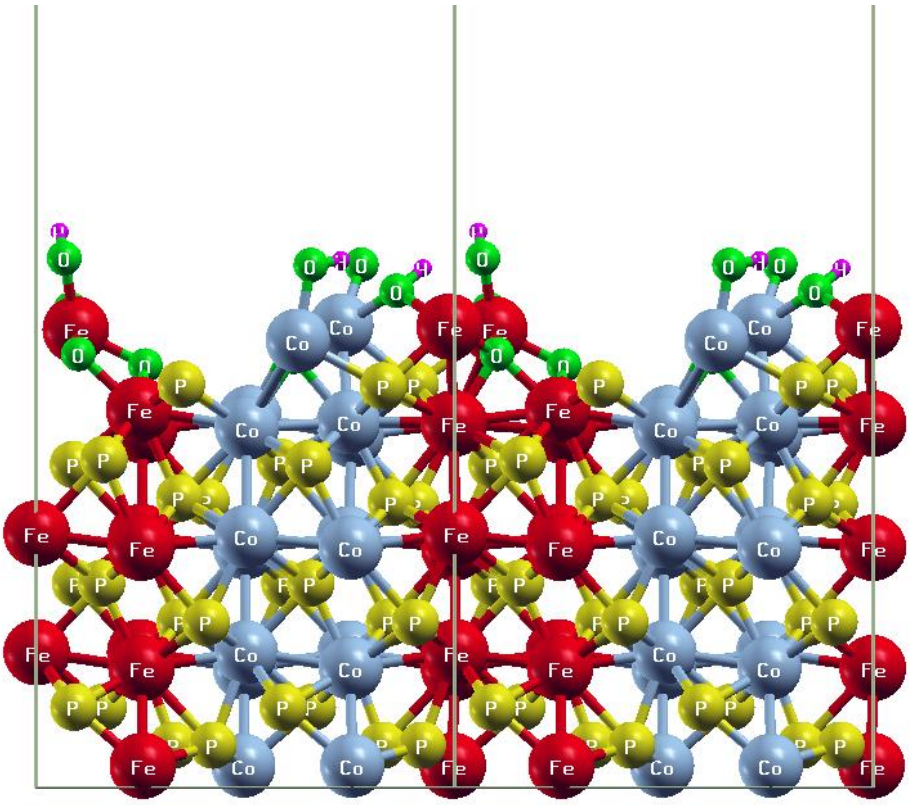

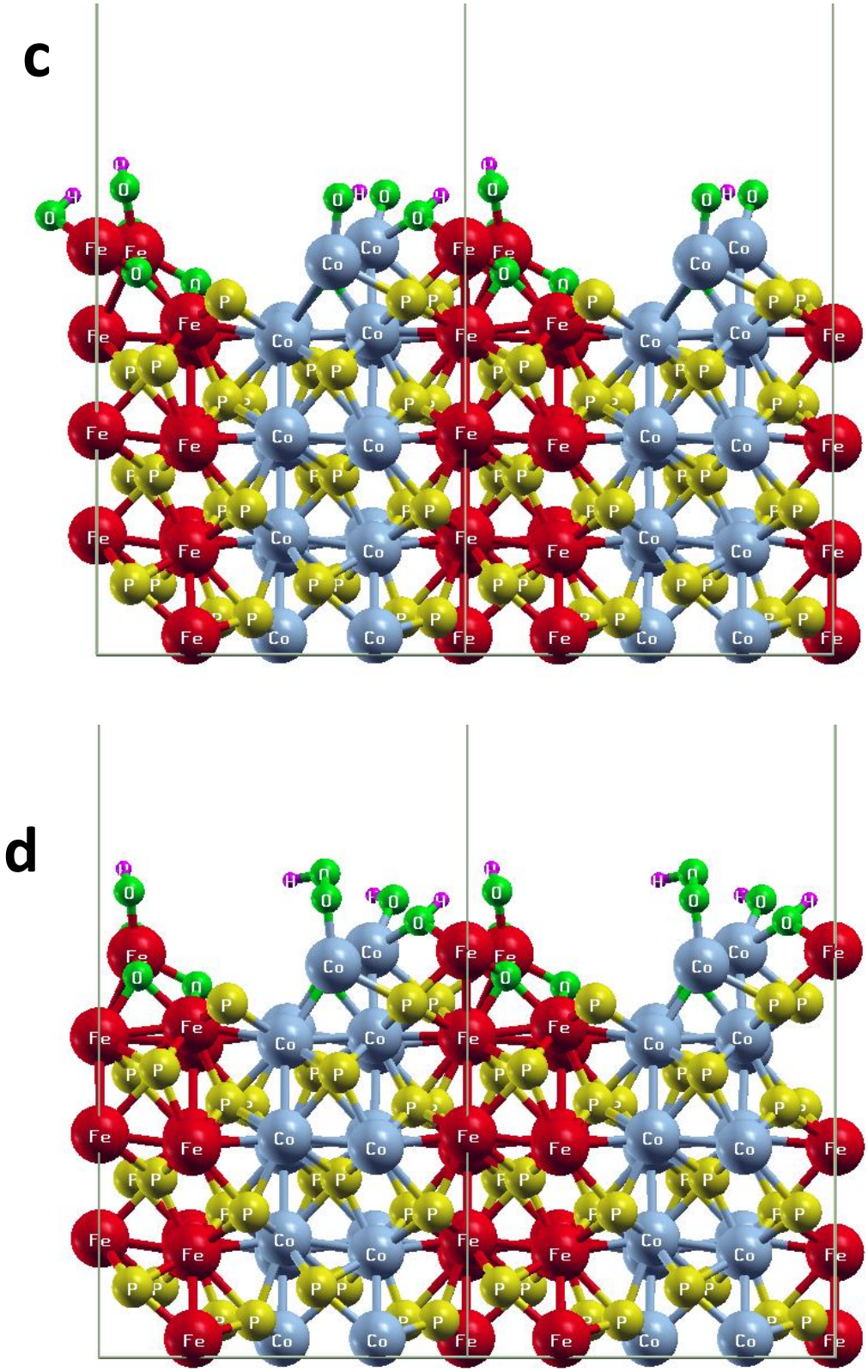

Fig. S44 (a) Relaxation of oxygenated surface on FeP-CoP interface, and (b-d) stable configurations of various intermediates (*OH, *O, *OOH) considering oxygenated surface on FeP-CoP interface with Co as the intermediate adsorption site.

a

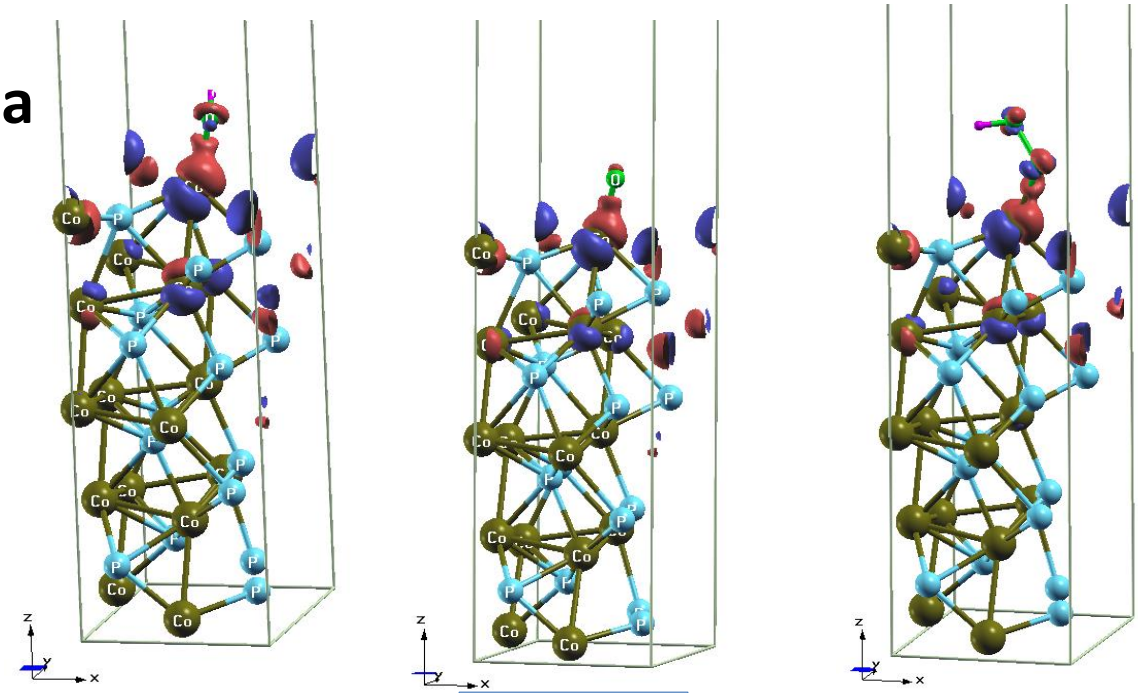

*OH	*O	*OOH
Isomin = - 0.62 Isomax = 0.52 Isovalue = 0.03	Isomin= - 0.96 Isomax = 0.82 Isovalue= 0.05	Isomin = - 0.28 Isomax = 0.26 Isovalue = 0.06

b

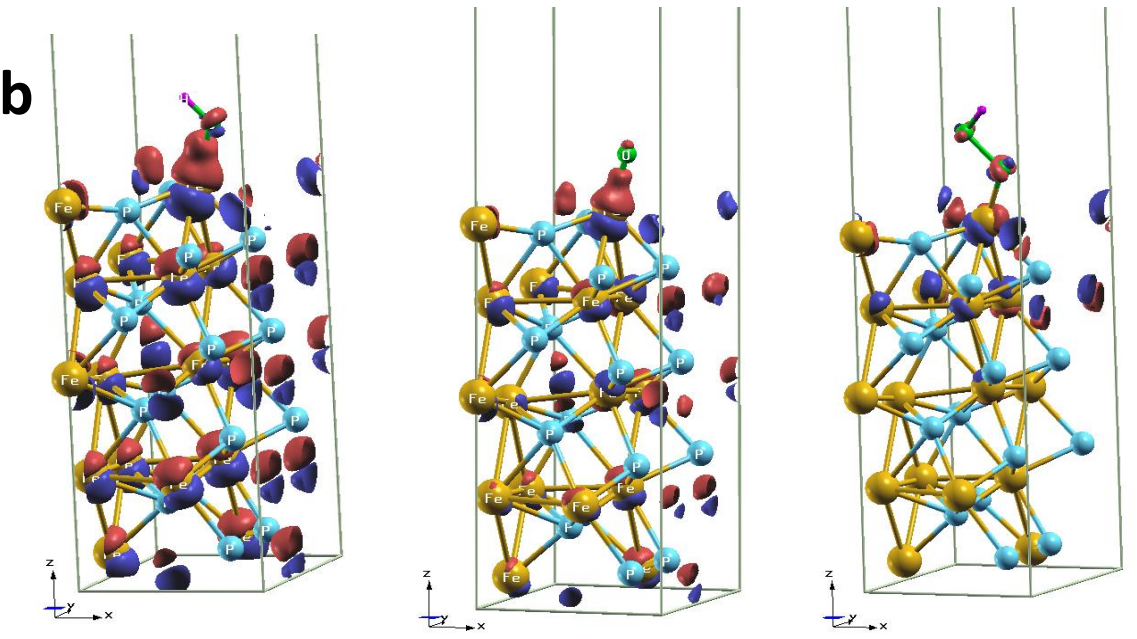

*OH	*O	*OOH
Isomin = - 0.62 Isomax = 0.52 Isovalue = 0.03	Isomin= - 0.65 Isomax = 0.48 Isovalue= 0.05	Isomin = - 0.28 Isomax = 0.26 Isovalue = 0.06

c

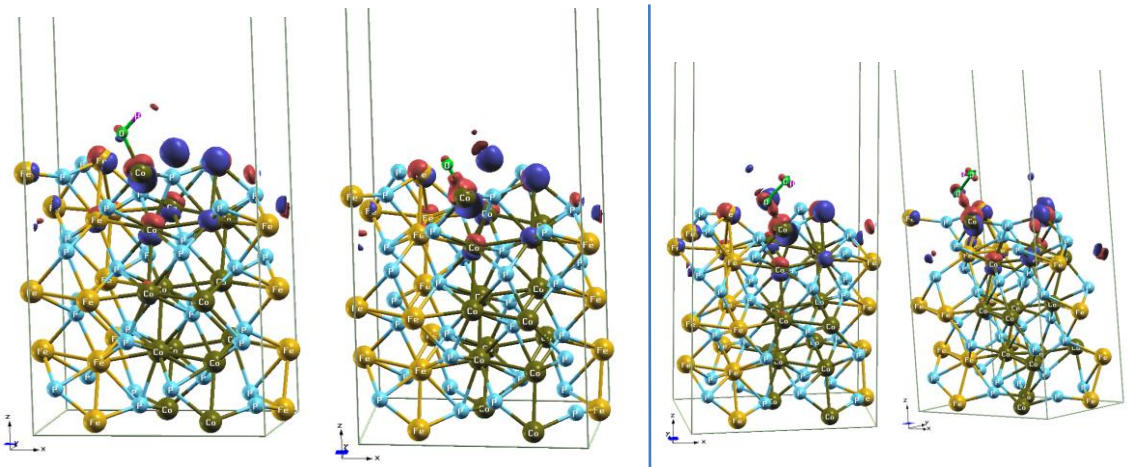

***OH**
Isomin= - 0.81
Isomax = 0.74
Isovalue= 0.04

***O**
Isomin= - 1.06
Isomax = 0.92
Isovalue = 0.05

***OOH**
Isomin= - 0.87
Isomax = 0.81
Isovalue= 0.04

d

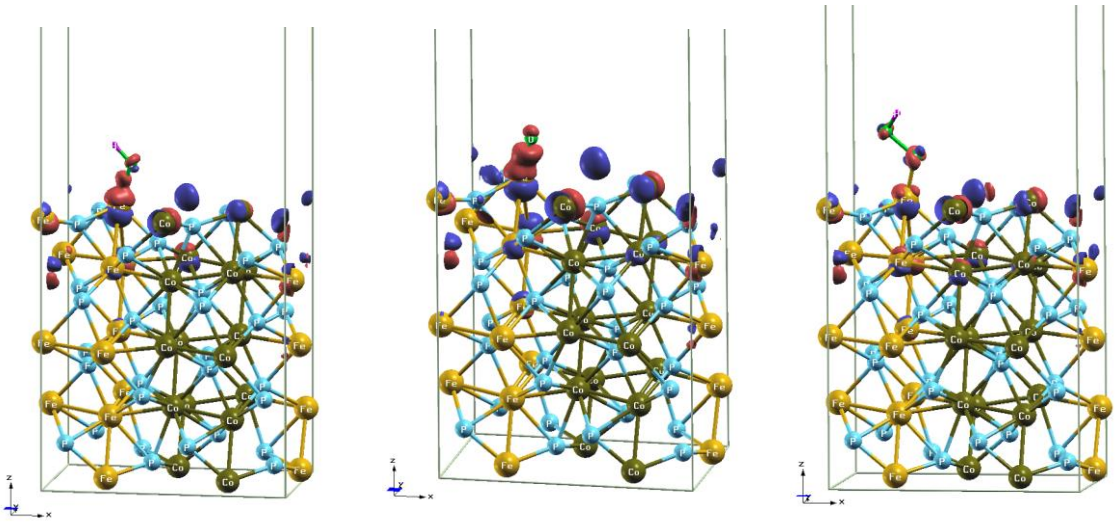

***OH**
Isomin= - 0.46
Isomax = 0.31
Isovalue= 0.03

***O**
Isomin= - 0.57
Isomax = 0.53
Isovalue= 0.03

***OOH**
Isomin= - 0.34
Isomax = 0.33
Isovalue= 0.04

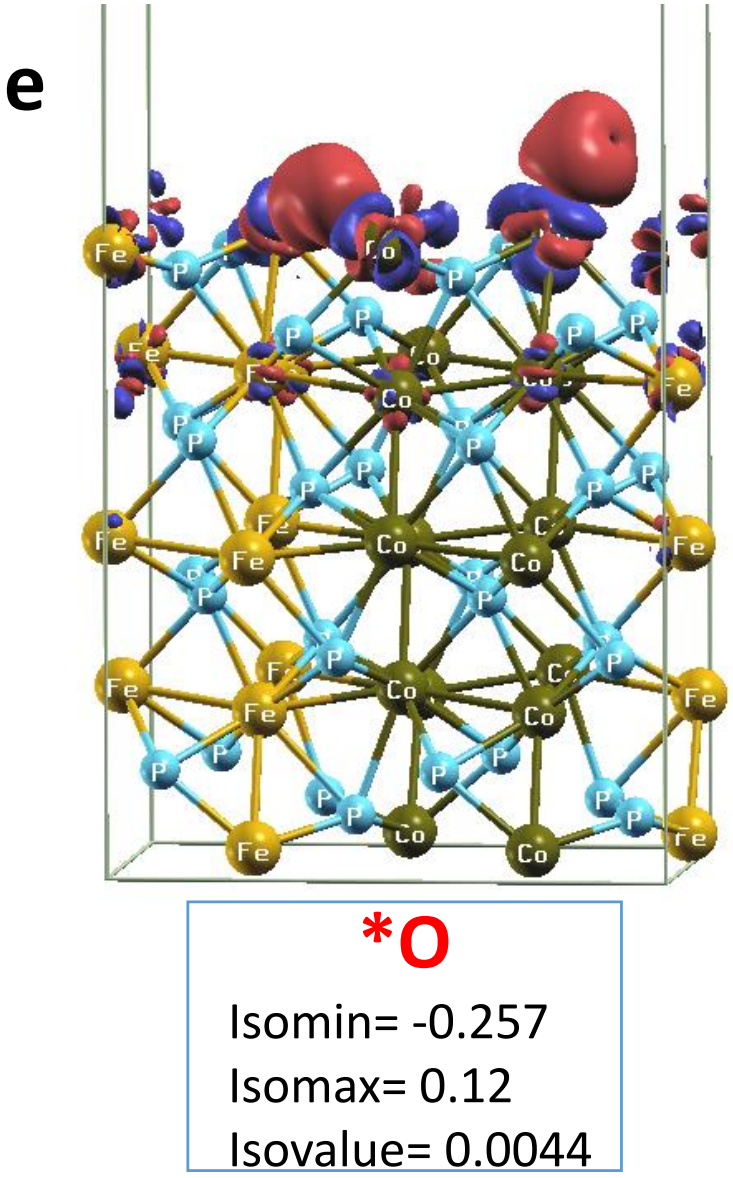

Fig. S45 (a) Charge density difference plots for (a) CoP (011) surface, (b) FeP (011) surface, (c) FeP-CoP interface (011) at Co site, and (d) FeP-CoP interface (011) at Fe site, and (e) O adsorption at FeP-CoP interface with one O atom.

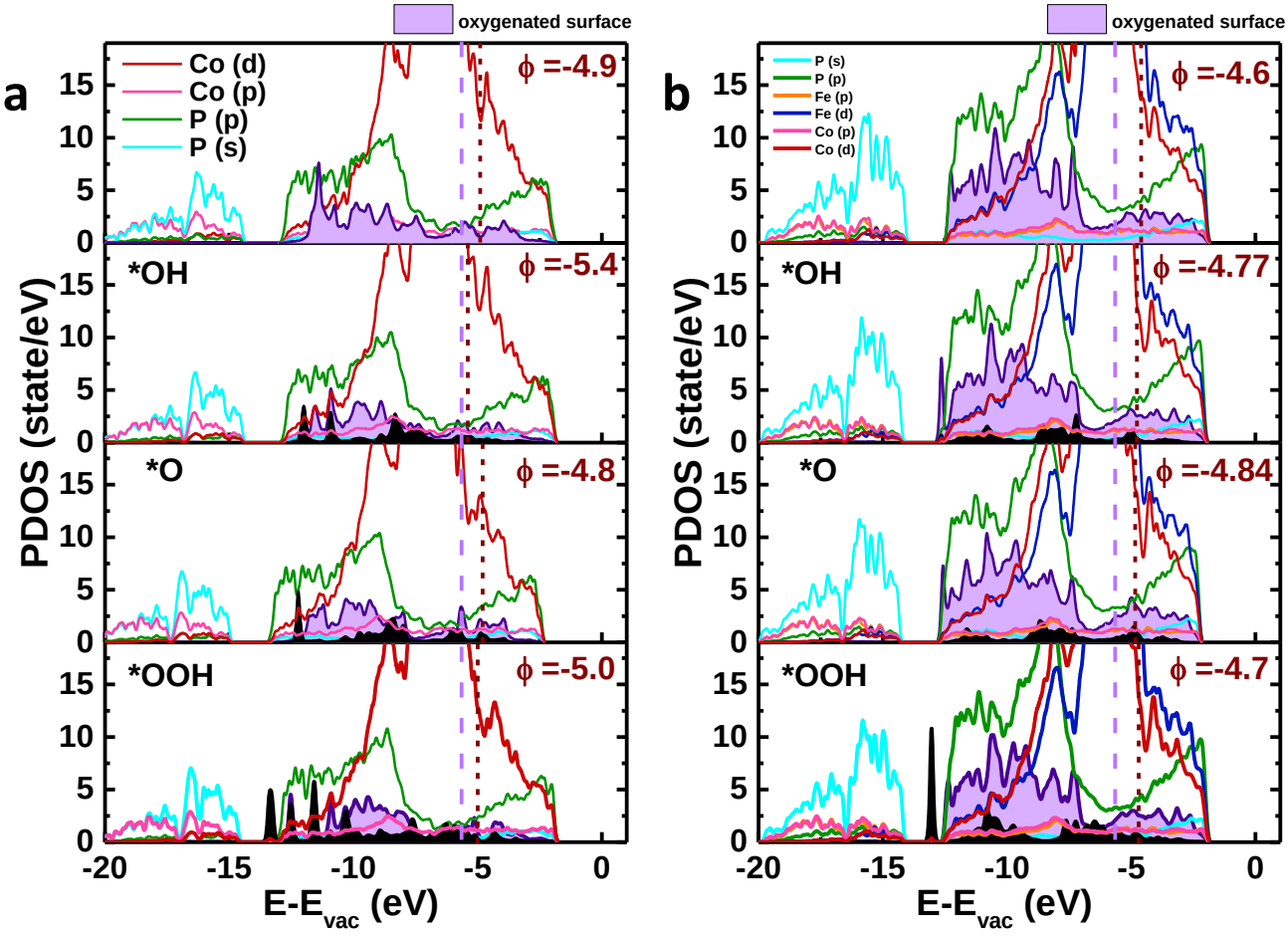

Fig. S46 Projected density of states (PDOS) of (a) oxygenated CoP, and (b) oxygenated FeP-CoP interface along with the adsorbed intermediates.

(The vertical violet line marks the OER potential at 5.67 eV and brown line denotes work function (ϕ). The black regions show density of states of adsorbed species.)

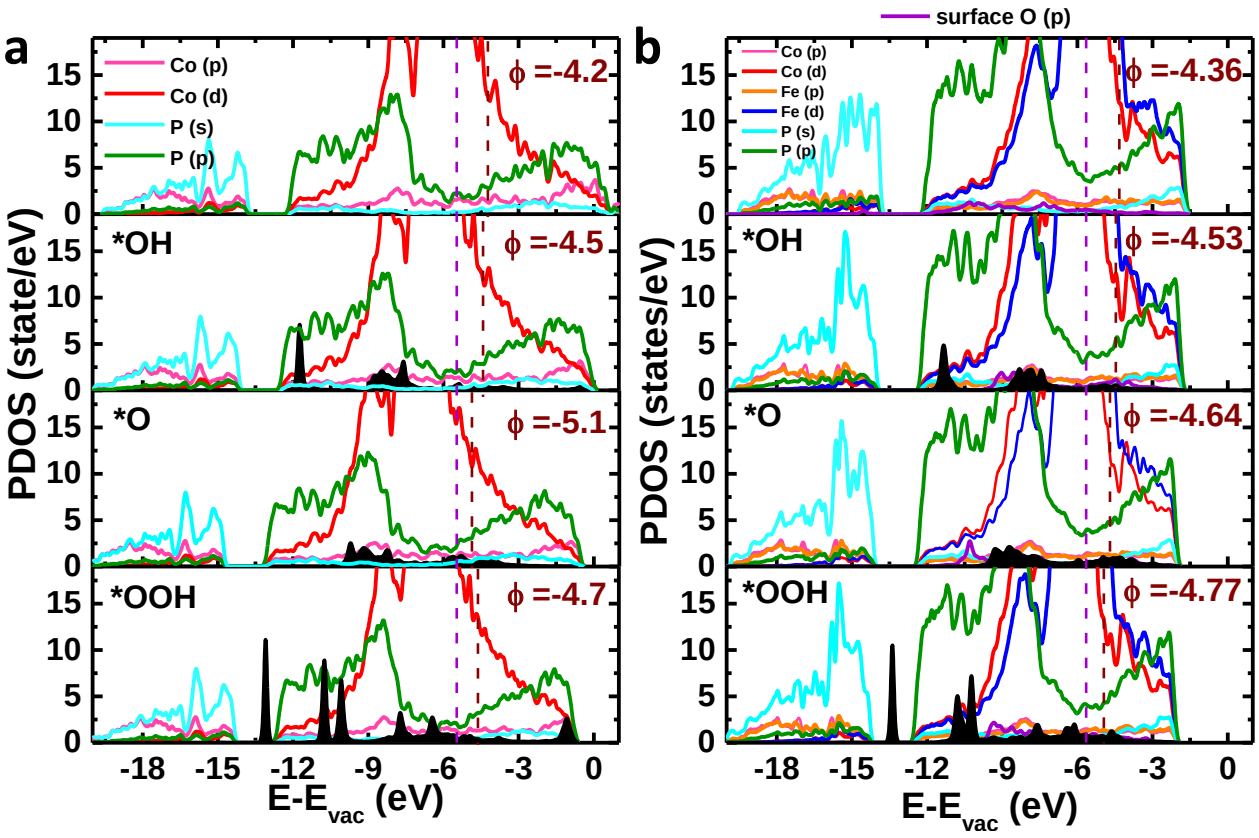

Fig. S47 Projected density of states (PDOS) of (a) pristine CoP, and (b) FeP-CoP interface with one surface oxygen along with the adsorbed intermediates.

(The vertical violet line marks the OER potential at 5.67 eV and brown line denotes work function (ϕ). The black regions show density of states of adsorbed species.)

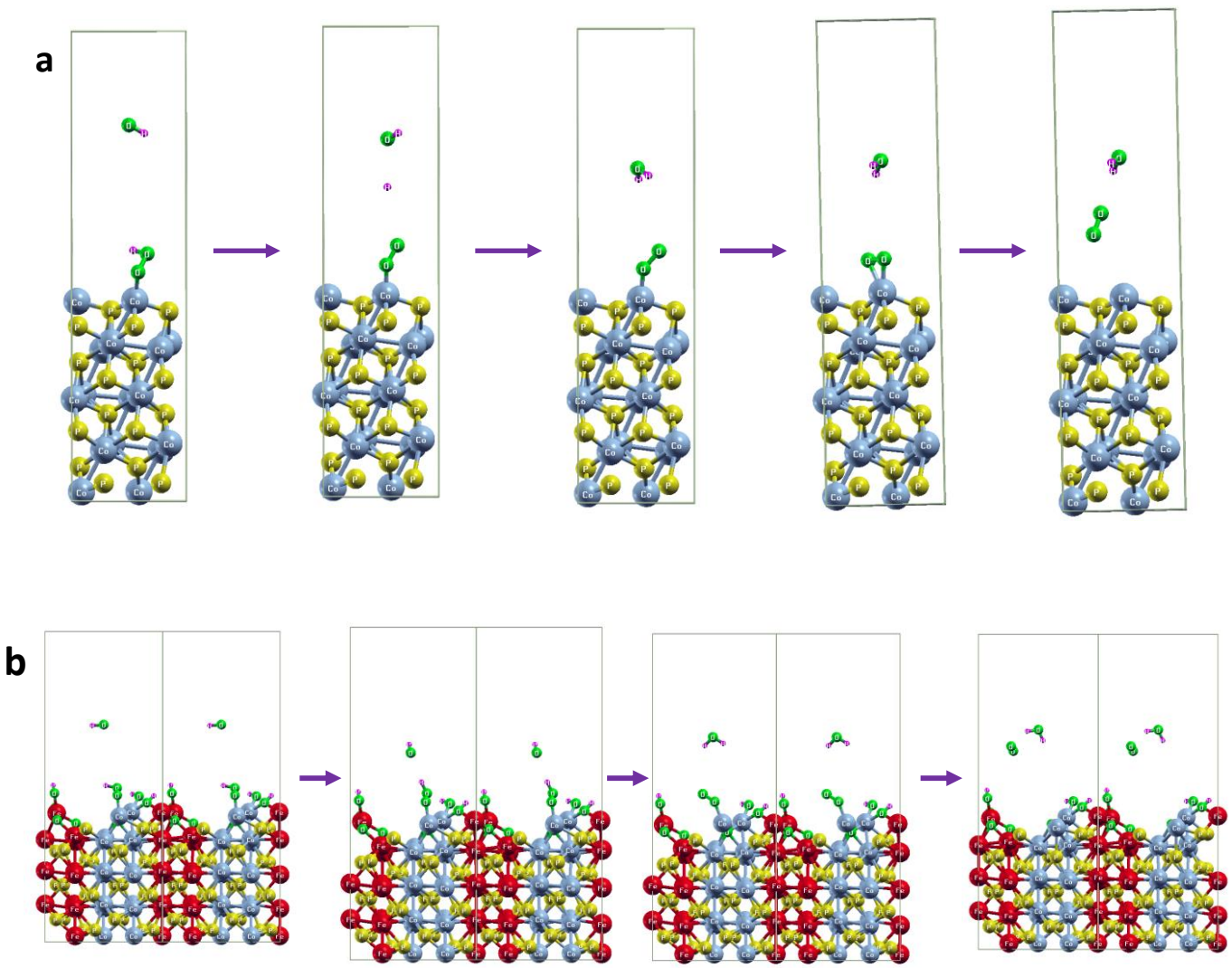

Fig. S48 NEB images for (a) final step of pristine CoP showing formation of O_2 and H_2O, and (b) showing barrierless formation of O_2 and H_2O on oxygenated surface of FeP-CoP interface.

1.6 Tables

Table T1. Binding energies of peaks corresponding to metal-phosphorus (M-P) bond observed from XPS analysis.

Catalyst	Binding Energies (eV)			
	Co		Fe	
	$2p_{3/2}$	$2p_{1/2}$	$2p_{3/2}$	$2p_{1/2}$
CoP	778.37	793.26	-	-
FeP	-	-	707.48	720.27
FeP-CoP	778.67	793.65	707.01	719.81

Table T2. Observed peak positions in Raman spectra.

CoP	FeP	FeP-CoP	CoFeP	FeP-CoP-AR
154	176	144-147	189	210-218
161	186	193-196	216	271-282
174-178	209-212	210	251	345
186-188	213-217	216	284	382-395
209	247-255	242	342	465-471
219	275-280	251-254	428	541-543
276	297	263-264	459	587-610
278	308	283	600	630-632
289	373	311	666	667-676
348	389-391	343-347		
364	418	364-365		
462-471	440-444	388-389		
504-511	592-595	416-419		
605-606		434		
663-675		458-461		
		512		
		594		
		662-667		

Peaks mentioned in green and violet colours correspond to cobalt and iron oxide species, respectively.

Table T3. OER performance of different metal phosphides.[16-39]

Catalyst [support]	Loading (mg cm^{-2})	Overpotential (mV) at (j)	Stability (h) at (j)	j (mA cm^{-2}) @ 500 mV	Tafel slope (mV dec^{-1})	Ref.
FeP-CoP [GCE]	0.112	220 (10)	200 (200)	1375	39.4	This work
CoP [GCE]	0.112	250 (10)	20 (200)	354	55.1	This work
FeP [GCE]	0.112	325 (10)	40 (200)	227	49.7	This work
IrO_2 [GCE]	0.112	283 (10)	35 (200)	320	62.6	This work
Co_2P@NPPC[a] [GCE]	0.35	316 (10)	10 (10)	40	98.0	15
CoFeBiP [NF]	0.31	273 (10)	25 (10)	90	77.3	16
CoP@FeNiP [NF]	8.0	283 (100)	110 (10)	-	31.8	17
Ni_2P@NSG[b] [NF]	5.0	240 (10)	60 (10)	-	47.0	18
CoFeP NS@Fe-CoP NW[c] [NF]	-	250 (30)	12 (34)	250	107.0	19
FeP_2-NiP_2 @PC[d] [GCE]	1.0	248 (10)	60 (40)	-	54.0	20
N-CoO@CoP [NF]	-	332 (100)	24 (100)	-	81.5	21
$NiSe_2$-Ni_2P [NF]	-	220 (50)	15 (60)	-		22
$Co(OH)_2$/Ag/ FeP [Ti foil]	-	236 (10)	50 (50, 100)	225	56	23
NiCoFeP/C [CP]	-	270 (10)	10 (10)	-	65	24

Table T3. (continued)

Catalyst [support]	Loading (mg cm^{-2})	Overpotential (mV) at (j)	Stability (h) at (j)	j (mA cm^{-2}) @ 500 mV	Tafel slope (mV dec^{-1})	Ref.
FeNiP/C [GCE]	0.68	229 (10)	-	-	74.5	25
FeNiP/PG[e] [CC]	2.0	229 (10)	10 (10, 50)	-	49.7	26
3 D $NiFeP_x$@ $NiCo_2P_4$ [NF}	-	230 (10)	10 (10)	250	-	27
CoP@PC[d] [CP]	1.0	280 (10)	20 (10)	-	53.0	28
Co_2P@ CoOOH [NF]	-	280 (10)	-	70	-	29
NiOOH/NiP [Zirconia mesh]	-	286 (10)	10 (15)	80	-	30
NiFeP [GCE]	-	330 (20)	10 (20)	60	39.0	31
$Co_{0.63}Fe_{0.21}P_{0.16}$ [CP]	-	217 (10)	15 (10, 50)	-	40.0	32
Fe-Ni_2P [GCE]	0.2	292 (10)	28 (10)	100	50.0	33
Fe_2P/CoP/Ni_5P_4-rGO [GCE]	0.204	232 (10)	24 (10)	-	47.0	34
FeP/Ni_2P [NF]	8.0	154 (10)	24 (100)	1500	22.7	35
CoMnP [GCE]	0.284	330 (10)	10 (10)		61.0	36
$Cu_3P_{0.75}Co_2P$ [NF]	2.0	334 (20)	-	150	132	37
Co-Fe-P-1.7 [NF]	0.42	244 (10)	30 (10)	250	58.0	38

NF: Nickel foam, GCE: glassy carbon electrode, CP: carbon paper, [a]NPPC: N, P co-doped porous carbon, [b]NSG: N, and S doped graphene, [c]NS: nanosheet, NW: nanowire, [d]PC: P doped carbon, [e]PG: P doped graphene.

Table T4. OER performance of CoP, FeP, (FeP-CoP), and IrO_2 catalysts.

Catalyst	Mass activity (@ 350, and 500 mV) ($A\ g^{-1}_{M}$)	ECSA (cm^2)	TOF (s^{-1})
(FeP-CoP)	4269, 18987	23.68	1.65
CoP	1290, 4893	14.84	0.54
FeP	374, 3257	11.49	0.27
IrO_2	572, 3264	1.74	0.66

Table T5. EIS circuit fitting parameters of different catalysts.

Circuit elements	FeP	CoP	(FeP-CoP)
R_u	0.001	0.001	0.001
Q_1	2.077 e-5	2.026 e-5	2.55 e-5
R_1	18.26	19.5	15.49
Q_2	0.98 e-3	2.75 e-3	4.9 e-3
R_2	19.71	10.78	7.037
C_3	17.14 e-5	2.15 e-5	8.75 e-5
R_3	27.64	24.7	7.49

Table T6. Metal oxidation peak position from CV studied in non-faradaic region of different catalysts.

Catalyst	Peak position (V vs. RHE)
CoP	0.995
(FeP-CoP)-(20:80)	1.038
(FeP-CoP)-(40:60)	1.045
(FeP-CoP)-(50:50)	1.070
(FeP-CoP)-(60:40)	1.103
(FeP-CoP)-(80:20)	1.145
FeP	1.170

Table T7. Charge carrier concentrations (N_a, and N_d) calculated from Mott-Schottky analysis.

Catalyst	Relative conc. of donor charge carrier (cm^{-3}), N_d	Relative conc. of acceptor charge carrier (cm^{-3}), N_a
FeP	1.03	1.0
CoP	1.83	1.86
FeP-CoP	2.09	2.81

Table T8. Surface energy of different catalysts.

Catalyst	Surface energy (kJ m^{-2})
CoP (011)	0.152
CoP (211)	0.103
FeP (011)	0.120
FeP (211)	0.085

Table T9. Adsorption energy and its contribution from Grimme-D2 corrections.

System	*O		*OH		*OOH	
	E_{ads} (eV)	E_{vdW} (eV)	E_{ads} (eV)	E_{vdW} (eV)	E_{ads} (eV)	E_{vdW} (eV)
CoP (011)	**-1.54**	**-0.08**	**-0.47**	**-0.13**	**-0.81**	**-0.18**
FeP (011)	**-2.50**	**-0.09**	**-0.91**	**-0.12**	**-1.32**	**-0.18**
FeP-CoP (011) at Co	**-1.74**	**-0.07**	**-0.50**	**-0.097**	**-0.94**	**-0.15**
FeP-CoP (011) at Fe	**-2.41**	**-0.11**	**-0.91**	**-0.13**	**-1.32**	**-0.18**
Oxygenated CoP	**-0.37**	**-0.09**	**-0.61**	**-0.24**	**-0.35**	**-0.31**
Oxygenated FeP-CoP interface	**-0.36**	**-0.07**	**-0.004**	**-0.20**	**-0.19**	**-0.24**

Table T10. Work functions for considered systems

System	Fermi level (E_F) (eV)	Vacuum Potential (eV)	Work function (ϕ) (eV)
CoP (011)	4.0135	8.255	4.2
***O at CoP (011)**	3.6252	8.779	5.1
***OH at CoP (011)**	3.9621	8.518	4.5
***OOH at CoP (011)**	3.9853	8.719	4.7
FeP (011)	3.6797	7.587	3.9
***O at FeP (011)**	3.2980	8.046	4.7
***OH at FeP (011)**	3.6666	7.754	4.1
***OOH at FeP (011)**	3.7614	7.772	4.0
FeP-CoP (011)	4.0429	8.104	4.1
***O at FeP-CoP (011) (Co site)**	3.8636	8.373	4.5
***OH at FeP-CoP (011) (Co site)**	4.0481	8.182	4.1
***OOH at FeP-CoP (011) (Co site)**	4.0361	8.337	4.3
FeP-CoP (011)	4.0429	8.104	4.1
***O at FeP-CoP (011) (Fe site)**	3.8440	8.336	4.5
***OH at FeP-CoP (011) (Fe site)**	4.0483	8.180	4.1
***OOH at FeP-CoP (011) (Fe site)**	4.1177	8.175	4.1
FeP-CoP (011) with one surface O	3.8872	8.2487	4.4
***O at FeP-CoP (011) with one surface O (Co site)**	3.8064	8.4477	4.6
***OH at FeP-CoP (011) with one surface O (Co site)**	3.8863	8.4168	4.5
***OOH at FeP-CoP (011) with one surface O (Co site)**	3.8354	8.6079	4.77
FeP-CoP (011) with two surface O	3.9085	8.3990	4.5
***O at FeP-CoP (011) with two surface O (Fe site)**	3.7973	8.6102	4.8
***OH at FeP-CoP (011) with two surface O (Fe site)**	3.9524	8.4464	4.5
***OOH at FeP-CoP (011) with two surface O (Fe site)**	3.9613	8.5704	4.6

1.7 References

1. S. Maity, D. K. Singh, D. Bhutani, S. Prasad, U. V. Waghmare, S. Sampath and E. Muthusamy, *Materials Research Bulletin*, 2021, **140**, 111312.
2. J. Xu, J. Li, D. Xiong, B. Zhang, Y. Liu, K. H. Wu, I. Amorim, W. Li and L. Liu, *Chem Sci*, 2018, **9**, 3470-3476.
3. Q. Liu, J. Tian, W. Cui, P. Jiang, N. Cheng, A. M. Asiri and X. Sun, *Angew Chem Int Ed Engl*, 2014, **53**, 6710-6714.
4. M. E. G. Lyons and M. P. Brandon, *Journal of Electroanalytical Chemistry*, 2010, **641**, 119-130.
5. R. L. Doyle and M. E. Lyons, *Phys Chem Chem Phys*, 2013, **15**, 5224-5237.
6. İ. B. Pehlivan, M. A. Arvizu, Z. Qiu, G. A. Niklasson and T. Edvinsson, *The Journal of Physical Chemistry C*, 2019, **123**, 23890-23897.
7. N. Sato, *Electrochemistry at Metal and Semiconductor Electrodes*, Sapporo, Japan, 1998.
8. M. Gao, X. Cao, Q. Gao, Y. Xu, Y. Zheng, J. Jiang and S. Yu, *ACS Nano*, 2014, **8**, 3970-3978.
9. R. Kothari, D. Buddhi and R. L. Sawhney, *Renewable and Sustainable Energy Reviews*, 2008, **12**, 553-563.
10. M. S. Burke, M. G. Kast, L. Trotochaud, A. M. Smith and S. W. Boettcher, *J. Am. Chem. Soc.*, 2015, **137**, 3638-3648.
11. P. Giannozzi, S. Baroni, N. Bonini, M. Calandra, R. Car, C. Cavazzoni, D. Ceresoli, G. L. Chiarotti, M. Cococcioni, I. Dabo, A. Dal Corso, S. de Gironcoli, S. Fabris, G. Fratesi, R. Gebauer, U. Gerstmann, C. Gougoussis, A. Kokalj, M. Lazzeri, L. Martin-Samos, N. Marzari, F. Mauri, R. Mazzarello, S. Paolini, A. Pasquarello, L. Paulatto, C.

Sbraccia, S. Scandolo, G. Sclauzero, A. P. Seitsonen, A. Smogunov, P. Umari and R. M. Wentzcovitch, *J Phys Condens Matter*, 2009, **21**, 395502.

12. X. Hua, X. Chen and W. A. Goddard III, *Physical Review B*, 1997, **55**, 16103-16109.
13. J. P. Perdew, K. Burke and M. Ernzerhof, *Physical Review Letters*, 1996, **77**, 3865-3868.
14. S. Grimme, *J Comput Chem*, 2006, **27**, 1787-1799.
15. P. Wisesa, K. A. McGill and T. Mueller, *Physical Review B*, 2016, **93**, 155109.
16. D. Li, Z. Li, J. Ma, X. Peng and C. Liu, *Sustainable Energy & Fuels*, 2021, **5**, 2477-2485.
17. C. Wang, H. Shang, Y. Wang, J. Li, S. Guo, J. Guo and Y. Du, *Nanoscale*, 2021, **13**, 7279-7284.
18. J. Wang, C. Chen, N. Cai, M. Wang, H. Li and F. Yu, *Nanoscale*, 2021, **13**, 1354-1363.
19. U. P. Suryawanshi, U. V. Ghorpade, D. M. Lee, M. He, S. W. Shin, P. V. Kumar, J. S. Jang, H. R. Jung, M. P. Suryawanshi and J. H. Kim, *Chemistry of Materials*, 2020, **33**, 234-245.
20. H. Bi, B. Li, J. Zhang, A. Pan, L. Jiang, G.-F. Huang, S.-L. Chang and W.-Q. Huang, *Applied Physics Letters*, 2021, **118**, 093901.
21. P. Ji, H. Jin, H. Xia, X. Luo, J. Zhu, Z. Pu and S. Mu, *ACS Appl Mater Interfaces*, 2020, **12**, 727-733.
22. M. Lu, L. Li, D. Chen, J. Li, N. I. Klyui and W. Han, *Electrochimica Acta*, 2020, **330**, 135210.
23. P. Wang, Z. Pu, W. Li, J. Zhu, C. Zhang, Y. Zhao and S. Mu, *Journal of Catalysis*, 2019, **377**, 600-608.
24. X. Ding, Y. Xia, Q. Li, S. Dong, X. Jiao and D. Chen, *ACS Appl Mater Interfaces*, 2019, **11**, 7936-7945.

25. X. Wei, Y. Zhang, H. He, L. Peng, S. Xiao, S. Yao and P. Xiao, *Chem Commun (Camb)*, 2019, **55**, 10896-10899.

26. X. Wang, L. Chai, J. Ding, L. Zhong, Y. Du, T. Li, Y. Hu, J. Qian and S. Huang, *Nano Energy*, 2019, **62**, 745-753.

27. F. Bu, W. Chen, M. F. Aly Aboud, I. Shakir, J. Gu and Y. Xu, *Journal of Materials Chemistry A*, 2019, **7**, 14526-14535.

28. Z. Wang, N. Heng, X. Wang, J. He and Y. Zhao, *Journal of Catalysis*, 2019, **374**, 51-59.

29. J. Wu, D. Wang, S. Wan, H. Liu, C. Wang and X. Wang, *Small*, 2020, **16**, e1900550.

30. H. Li, Q. Li, P. Wen, T. B. Williams, S. Adhikari, C. Dun, C. Lu, D. Itanze, L. Jiang, D. L. Carroll, G. L. Donati, P. M. Lundin, Y. Qiu and S. M. Geyer, *Adv Mater*, 2018, **30**, 1705796.

31. X. Xu, C. Li, J. G. Lim, Y. Wang, A. Ong, X. Li, E. Peng and J. Ding, *ACS Appl Mater Interfaces*, 2018, **10**, 30273-30282.

32. H. W. Man, C. S. Tsang, M. M. Li, J. Mo, B. Huang, L. Y. S. Lee, Y. C. Leung, K. Y. Wong and S. C. E. Tsang, *Chem Commun (Camb)*, 2018, **54**, 8630-8633.

33. T. Wang, C. Wang, Y. Jin, A. Sviripa, J. Liang, J. Han, Y. Huang, Q. Li and G. Wu, *Journal of Materials Chemistry A*, 2017, **5**, 25378-25384.

34. G. Liu, D. He, R. Yao, Y. Zhao and J. Li, *Electrochimica Acta*, 2017, **253**, 498-505.

35. Y. Du, J. Chen, L. Li, H. Shi, K. Shao and M. Zhu, *ACS Sustainable Chemistry & Engineering*, 2019, **7**, 13523-13531.

36. F. Yu, H. Zhou, Y. Huang, J. Sun, F. Qin, J. Bao, W. A. Goddard, 3rd, S. Chen and Z. Ren, *Nat Commun*, 2018, **9**, 2551.

37. D. Li, H. Baydoun, C. N. Verani and S. L. Brock, *J Am Chem Soc*, 2016, **138**, 4006-4009.

38. L. Liu, L. Ge, Y. Sun, B. Jiang, Y. Cheng, L. Xu, F. Liao, Z. Kang and M. Shao, *Nanoscale*, 2019, **11**, 6394-6400.

39. T. Zhang, J. Du, P. Xi and C. Xu, *ACS Appl Mater Interfaces*, 2017, **9**, 362-370.